A Novel Algorithm Based on Compressive Sensing to Mitigate Phase Unwrapping Errors in Multitemporal DInSAR Approaches

Michele Manunta and Muhammad Yasir

***Abstract*— In this work, we present a new method based on the compressive sensing (CS) theory to correct phase unwrapping (PhU) errors in the multitemporal sequence of interferograms exploited by advanced differential interferometric synthetic aperture radar (DInSAR) techniques to generate deformation time series. The developed algorithm estimates the PhU errors by using a modified L_1-norm estimator applied to the interferometric network built in the temporal/spatial baseline plane. Indeed, in order to search the minimum L_1-norm sparse solution, we apply the iterative reweighted least-squares method with an improved weight function that takes account of the baseline characteristics of the interferometric pairs. Moreover, we also introduce a quality function to identify those solutions that have no physical meaning. Although the proposed approach can be applied to different multitemporal DInSAR approaches, our analysis is tailored to the full-resolution small baseline subset (SBAS) processing chain that we properly modify to implement the proposed CS-based algorithm. To assess the performance of the developed technique, we carry out an extended experimental analysis based on simulated and real SAR data. In particular, we process two wide SAR datasets acquired by Sentinel-1 and COSMO-SkyMed constellations over central Italy between 2011 and 2019. The achieved experimental results clearly demonstrate the effectiveness of the developed approach in retrieving PhU errors and generating displacement time series related to strongly nonlinear deformation phenomena. Indeed, the developed CS-based technique significantly increases the number of detected coherent points and improves the accuracy of the retrieved deformation time series.**

***Index Terms*— Compressive sensing (CS), differential synthetic aperture radar interferometry (DInSAR), phase unwrapping (PhU), small baseline subset (SBAS).**

Manuscript received August 17, 2020; revised December 23, 2020 and April 13, 2021; accepted April 23, 2021. Date of publication May 25, 2021; date of current version January 5, 2022. This work was supported in part by the ENVRIFAIR Project of the European Union Horizon 2020 for Research and Innovation Program under Grant Agreement 824068, in part by the I-AMICA Project under Grant PONa3_00363, and in part by the Istituto per il Rilevamento Elettromagnetico dell'Ambiente (IREA)-Italian National Research Council (CNR)/Italian Ministry of Economic Development DGS-UNMIG Agreement. *(Corresponding author: Michele Manunta.)*

Michele Manunta is with the Italian National Research Council (CNR)-Istituto per il Rilevamento Elettromagnetico dell'Ambiente (IREA), 80124 Naples, Italy (e-mail: manunta.m@irea.cnr.it).

Muhammad Yasir is with the Italian National Research Council (CNR)-Istituto per il Rilevamento Elettromagnetico dell'Ambiente (IREA), 80124 Naples, Italy, and also with the Department of Engineering, University of Naples "Parthenope," 80143 Naples, Italy (e-mail: yasir.m@irea.cnr.it).

This article has supplementary downloadable material available at https://doi.org/10.1109/TGRS.2021.3079158, provided by the authors.

Digital Object Identifier 10.1109/TGRS.2021.3079158

I. Introduction

THE advanced differential synthetic aperture radar (SAR) interferometry (DInSAR) [1]–[3] techniques are multitemporal approaches that allow the generation of deformation time series through the processing of large stacks of SAR interferograms relevant to an area of interest of the Earth's surface [4]–[13]. Although the several multitemporal DInSAR techniques can differ for a number of specific technical and implementation details, all these techniques have to deal with the phase unwrapping (PhU) operation [14] to retrieve the unwrapped phase of each analyzed SAR pixel in the considered differential interferograms. PhU can be effectively tackled by applying different approaches (i.e., spatial, temporal, 3-D, or other combination of spatial and temporal PhU methods); however, as PhU is an ill-posed problem, regardless of the used solution method, the PhU errors still represent an open issue in any multitemporal DInSAR approach, which can negatively impact the accuracy of the retrieved deformation time series. Indeed, despite that the PhU methods, developed in the last two decades, reached a high level of efficiency, the PhU errors can jeopardize the correct reconstruction of the deformation time series relevant to significantly nonlinear displacement signals, such as those related to seismic events, volcanic unrest episodes, and anthropogenic-related hazards. Due to the impact that PhU errors have in the generation of deformation time series, several methods were developed for their mitigation in multitemporal DInSAR approaches. Yang *et al.* [15] and Ojha *et al.* [16] propose two techniques based on a region growing strategy, whereas, in [17], the proposed method, based on space constraints, is a bridging scheme to automatically connect reliable regions using tree searching algorithms. Finally, some approaches exploit the L_1-norm to mitigate the impact of the PhU errors on the DInSAR time series [18]–[20].

In this work, we propose a new method based on the compressive sensing (CS) theory to estimate and mitigate the PhU errors in the interferograms exploited within the multitemporal DInSAR approaches. Due to the characteristics of the most recent SAR systems (reduced revisit time and short orbital tube) that allow us to generate interferograms with reduced spatial and temporal decorrelation phenomena [21], the number of PhU errors that affect coherent points is often very small with respect to the number of the used interferometric pairs. This means that, from a mathematical

point of view, the vector associated with the PhU errors can be considered sparse.

An effective way to address inverse problems characterized by sparse solutions, as for the case of PhU errors estimation in multitemporal DInSAR approaches, is to apply the CS theory. Compressive (or compressed) sensing (CS) is a relatively new signal processing approach that, under appropriate conditions, allows robust and stable reconstruction of signals from an undersampled set of noisy measurements [22], [23]. Generally speaking, CS is based on the sparsity concept to solve L_0-norm minimization problems by using L_1-norm methods. Indeed, L_0 minimization problems occur in several scientific fields, but their solution is hard to find (computer science defines this class of problems NP-hard [24], [25]). The CS theory demonstrates that, when the solution of the L_0 problem is a sparse vector, i.e., a vector where the number of nonzero elements is significantly smaller than the number of its elements, the L_0 minimization problem can be converted in an equivalent, and easier, L_1 problem if some matrix conditions and properties are satisfied. Indeed, unlike L_0-norm minimization problems, those L_1 can be effectively addressed by utilizing solvers based on linear programming or iterative methods [22]. The CS principles have been successfully applied in several contexts related to SAR processing and applications [26]–[31]. However, even if some works investigated the use of L_1-norm minimization methods for multitemporal DInSAR applications [18]–[20], the full exploitation of CS techniques in multitemporal DInSAR approaches is broadly unexplored.

In this work, we present an effective way to benefit from CS theory in the multitemporal DInSAR techniques. In particular, the developed algorithm can be applied to correct interferograms unwrapped with any PhU method and the only requirement concerns the selection of the interferometric pairs that have to be based on a triangulated network. The procedure is based on a pixel-by-pixel analysis, i.e., all pixels are analyzed independently of each other; therefore, the pixels can be computed in parallel. The algorithm is then intrinsically suitable to be implemented through parallel programming techniques to reduce its computing time.

To demonstrate the effectiveness of the proposed algorithm, among the several multitemporal DInSAR approaches, we tailor our method to the small baseline subset (SBAS) processing chain [4], [5] that is a well-known algorithm able to reconstruct deformation time series with centimeter to millimeter accuracy [32]–[34]. The SBAS algorithm has initially been proposed to retrieve low-to-medium spatial resolution DInSAR products (i.e., deformation time series and mean velocity maps) relevant to very extended areas [35], [36] by processing multilook interferograms. Later, the SBAS approach has been extended to work on full-resolution (FR) SAR interferograms to retrieve high-resolution deformation time series [5]. The FR SBAS algorithm has been then enhanced to jointly process SAR data acquired by different satellite systems characterized by slightly different carrier frequencies, as for the case of the ERS-1/2 and ASAR-ENVISAT systems [37].

The FR SBAS algorithm allows retrieving deformation phenomena that characterize both natural and anthropogenic hazards, such as seismic events, volcanic unrest, landslides, faults, urban areas, and single man-made infrastructures. It has been used and successfully applied in several application scenarios, and its accuracy has been assessed by benefitting from independent ground-based measurements [32], [33], [36], [38]–[46].

The rationale of the FR SBAS algorithm is quite simple as it is effective; it is based on a two-scale approach referred to as regional (or large) and local spatial scale analyses.

1) The regional-scale analysis is carried out by processing multilook interferograms through the P-SBAS processing chain [47]–[49]. The interferometric stack is unwrapped and subsequently inverted through the singular value decomposition (SVD) method to retrieve medium resolution products, such as deformation time series, atmospheric phase screen contribution, and DEM and orbital errors.
2) The local-scale analysis uses single-look interferograms and is carried out on a pixel-by-pixel basis; after a high-pass (HP) spatial filtering, the HP phase component is processed by estimating the linear terms, i.e., the deformation velocity and topographic phase. Finally, the nonlinear deformation phase term is retrieved by applying the SVD method. This latter operation is carried out by assuming that the nonlinear phase component ranges in the $[-\pi, \pi)$ interval, and no additional PhU operation is needed.

The overall FR SBAS products are finally achieved by adding up regional- and local-scale SBAS products.

By benefiting from the proposed CS-based PhU errors estimator, we modify the FR SBAS processing chain to estimate the PhU errors that are mainly associated with strongly nonlinear deformation patterns. In particular, we apply our CS-based approach in two different points of the FR SBAS processing chain.

1) In the regional-scale analysis, we estimate and mitigate 2π multiples errors that affect the unwrapped multilook interferograms.
2) In the local-scale analysis, we unwrap the nonlinear phase component with no assumption that such a component is small enough to be considered unwrapped in the $[-\pi, \pi)$ interval.

In this article, we firstly analyze the main theorems of CS, in order to investigate how and when the CS approach can be effectively applied to the PhU problem. In particular, we show that, although it cannot be always solved with the CS, this latter provides the optimal or suboptimal solution in a large number of real cases. Moreover, to enhance the capability of the proposed approach to retrieve the PhU errors, we present an L_1 estimator that we have properly modified to improve its performances on real DInSAR cases. Subsequently, the tailoring of the proposed algorithm to the FR-SBAS processing chain is presented. Finally, we carry out a deep experimental analysis based on both simulated and real data to assess the performance of the proposed approach. More in detail, we use a TOPS Sentinel-1 dataset made of 171 images acquired over Central Italy between March 2015 and December 2018; by exploiting this dataset, we perform the experimental analysis on real data to assess the results of the CS-enhanced

regional-scale SBAS approach. The second analysis is based on a Stripmap COSMO-SkyMed (CSK) dataset acquired over the city of Rome, Italy, from March 2011 to March 2019. The CSK dataset, composed of 129 scenes, is analyzed with the local-scale SBAS approach, properly modified with the proposed CS method, and the deformations affecting the city of Rome are retrieved at the full spatial-resolution scale.

II. Compressive Sensing in a Nutshell

The compressive (or compressed) sensing theory is a relatively new signal processing approach originally proposed by Donoho [23] and Candès *et al.* [50] since 2004. An overall and up-to-date overview of the CS theory and implementation can be found in [22]. Generally speaking, CS exploits the sparsity of the signals to reconstruct their expression from a small set of measurements or samples. Before analyzing some key achievements of CS, for the sake of completeness, it is important to introduce some basic concepts largely used in CS. First, CS is applied to L_0-norm optimization problems, where the L_p-norm of a vector $x \in \mathbb{R}^m$ is defined as follows:

$$L_p : \|x\|_p = \sqrt[p]{\sum_{i=1}^{m} |x_i|^p} \quad \forall\ 1 \leq\ p < \infty. \tag{1}$$

It is worth noting that, even if it is always used in this sense, L_0 is actually not a norm (for example, $\|\alpha x\|_0 \neq \alpha \|x\|_0$); it corresponds to the number of nonzero elements of a vector

$$\|x\|_0 = \text{card}\{\text{x}_i : \text{x}_i \neq 0\}. \tag{2}$$

Moreover, CS makes use of the concept of sparsity: a vector is defined as k-sparse if

$$\|x\|_0 = k \quad \text{and } k \ll m. \tag{3}$$

Generally speaking, a vector is defined as sparse when the number of nonzero elements is significantly smaller than the number of the vector elements, i.e., when $\text{card}\{\text{x}_i : \text{x}_i \neq 0\} \ll \text{card}\{x\}$.

Let us now suppose[1] to have a signal $x \in \mathbb{R}^m$ that is undersampled according to (4)

$$y = \boldsymbol{A}x \tag{4}$$

where $\boldsymbol{A} \in \mathbb{R}^{n \times m}$, $y \in \mathbb{R}^n$, and $n \ll m$. (4) is an undetermined system of linear equations and has an infinite number of possible solutions. However, if x can be represented as a linear combination of a sparse signal $s \in \mathbb{R}^n$ and $\|s\|_0 = k$

$$x = \boldsymbol{\Psi} s \tag{5}$$

where $\boldsymbol{\Psi} \in \mathbb{R}^{m \times n}$, and the original signal x can be effectively reconstructed by solving (6)

$$\hat{s} = \arg\min \|s\|_0 \quad \text{subject to y} = \boldsymbol{C}s \text{ with } \boldsymbol{C} = \boldsymbol{A\Psi} \tag{6}$$

where $\hat{s}$ is the estimate of s.

Unfortunately, finding the solution of (6) is not a trivial problem because L_0-norm has no mathematical representation; indeed, L_0 minimization is computationally very expensive and is regarded by computer science as an NP-hard problem [24], [25], i.e., in terms of computational complexity, it is not manageable.

[1]The following analysis is carried out on real numbers $\mathbb{R}$ but can be easily extended to complex numbers C.

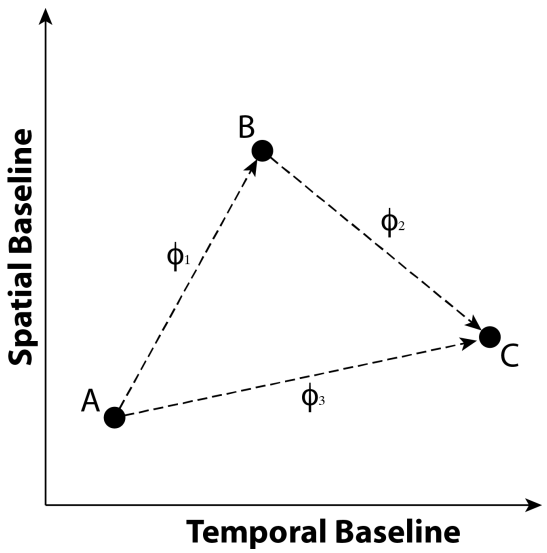

Fig. 1. Simple scenario where three acquisitions are paired in a triangulation form.

In this framework, the CS theory demonstrates that, under appropriate conditions, it is possible to reconstruct the sparse vector $\hat{s}$ from the vector of measurements y by solving the following problem:

$$\hat{s} = \arg\min \|s\|_1 \quad \text{s.t. } y = \boldsymbol{C}s. \tag{7}$$

Converse to L_0 optimization problems, L_1 ones can be effectively addressed by utilizing solvers based on linear programming or iterative methods. In literature, several algorithms to solve (7), such as convex and nonconvex optimization, greedy, thresholding, Bayesian, and combinatorial approaches, can be easily found. A detailed analysis of the several solving algorithms has been carried out in [22].

As previously anticipated, a unique and sparse solution of (6) exists and can be achieved by solving (7) if some conditions are satisfied. First, a minimum number $N = O(k \log(m/k))$ of measurements is needed. Second, a sufficient (not necessary) condition on $\boldsymbol{C}$ matrix is the restricted isometry property (RIP) [23]

$$(1 - \delta_k) \leq \frac{\|\boldsymbol{C}u\|_2^2}{\|u\|_2^2} \leq (1 + \delta_k) \quad \forall\ u \in \mathbb{R}^n |\ \|u\|_0 = k. \tag{8}$$

The matrix $\boldsymbol{C}$ satisfies the k-order RIP condition when a value of $\delta_k \in (0, 1)$ that fulfills (8) exists; δ_k is defined restricted isometry constant (RIC): the smaller the δ_k, the better the reconstruction of the sparse signal in the presence of noise.

III. Compressive Sensing and Phase Unwrapping Errors

Let us now consider three SAR acquisitions A, B, and C (see Fig. 1) acquired at time t_A, t_B, and t_C, respectively. The associated interferograms, say ϕ_1, ϕ_2, and ϕ_3, are created

by pairing acquisitions A and B, B and C, and A and C, respectively. When dealing with correctly unwrapped phase measurements, the triangle shown in Fig. 1 must exhibit irrotational property, i.e., for any point of coordinates (x, r), we can write

$$\phi_1(x,r) + \phi_2(x,r) - \phi_3(x,r) = 0. \tag{9}$$

Now, let us consider an SAR dataset of $N+1$ acquisitions acquired at the ordered times $\boldsymbol{t} = [t_0, t_1, \ldots, t_N]$, from which a list of M small baseline interferometric pairs can be extracted; an effective way to select the interferometric pairs has been proposed in [51], where the Delaunay triangulation method is applied in the temporal/spatial baseline plane. Accordingly, (9) can be easily extended to the $N+1$ acquisitions case where a system of Q linear equations is defined, where Q represents the number of triangles in the temporal/spatial baseline plane. Therefore, (9) can be easily organized in matrix form as follows:

$$\boldsymbol{C}\phi = 0 \tag{10}$$

where $\boldsymbol{C}$, hereafter referred to as triangulation matrix, is a sparse matrix of order $Q \times M$ and $Q < M$.

In the presence of PhU errors, (10) can be violated over a set of interferograms affected by PhU errors

$$\boldsymbol{C}\hat{\phi} \neq 0 \tag{11}$$

that can be rewritten in the following form:

$$\boldsymbol{C}\left(\hat{\phi} - 2\pi \cdot \varepsilon\right) = 0, \quad \text{with } \varepsilon \in \mathbb{Z}^M \tag{12}$$

where $\boldsymbol{\varepsilon}$ represents the vector of PhU errors; (12) is equivalent to

$$\boldsymbol{C}\varepsilon = \frac{1}{2\pi}\boldsymbol{C}\hat{\phi} \tag{13}$$

which identifies a system of Q independent equations, M unknowns, and ∞^{M-Q} solutions.

Since we can reasonably suppose that, among all the possible solutions of (13), the most physically realistic one provides the minimum number of 2π errors, and the solution of (13) is given by the following minimization problem:

$$\min\|\varepsilon\|_0 \quad \text{s.t. } \boldsymbol{C}\varepsilon = \phi^{tr} \text{ with } \phi^{tr} = \frac{1}{2\pi}\boldsymbol{C}\hat{\phi}. \tag{14}$$

As discussed in Section II, solving (14) is not a trivial problem; anyway, by benefiting from the CS theory, the class of problems as (14) can be effectively reduced to L_1 minimization problem if the solution $\boldsymbol{\varepsilon}$ is a sparse vector, i.e., in our case, when the number k of unwrapping errors is significantly smaller than the number of interferograms

$$\|\varepsilon\|_0 = k \ll M. \tag{15}$$

Accordingly, following the analysis presented in Section II, (14) becomes:

$$\min\|\varepsilon\|_1 \quad \text{s.t. } \boldsymbol{C}\varepsilon = \phi^{tr} \tag{16}$$

that can be formulated as a linear programming problem [23]. However, before applying the CS approach and stating that (16) provides the unique sparse solution, we have to verify that some conditions are satisfied.

First, the minimum number Q of needed measurements (triangles) is [29]

$$Q = O\left(k \log\left(\frac{M}{k}\right)\right). \tag{17}$$

Considering the small value of k, (17) is easily fulfilled. However, large values of Q (number of measurements) are recommended. Although the proposed approach is not intrinsically limited to work with networks triangulated in the temporal/spatial baseline plane and can be implemented also pairing the SAR images with quadrilateral or other geometrical shapes, it is easy to show that, given a dataset of $N+1$ SAR images, a network based on triangles guarantees the largest ratio (Q/M) between the numbers of equations and unknowns because the number of equations (Q) grows faster than the number of unknowns (M) when the number of polygon sides decreases (e.g., when the network includes only one polygon with $N+1$ sides, we have $(Q/M) = 1/(N+1)$.

Second, the RIP condition in (8) has to be checked to guarantee a robust solution in the presence of noisy measurements. It has been found in the literature that demonstrating (8) for an arbitrary matrix $\boldsymbol{C}$ is an NP-hard problem [52]. However, it is possible to show that, although, in our problem, matrix $\boldsymbol{C}$ never satisfies the RIP condition, we have a small enough RIC in a significant number of cases where CS, then, can be successfully applied. Accordingly, we have a high probability to solve our problem with CS methods.

To show this, (8) can be written as a system of inequalities

$$\begin{cases} \delta_k \geq 1 - \mu \\ \delta_k \geq \mu - 1 \\ \delta_k \in (0,1) \end{cases} \quad \forall\ \mu = \frac{\|\boldsymbol{C}u\|_2^2}{\|u\|_2^2} \tag{18}$$

whose solution is represented by the points belonging to the area shaded in red in Fig. 2 $(0 < \mu < 2)$.

To show that, in our problem, (18) is never satisfied for any value of k, let us consider some possible distributions of PhU errors. In Fig. 3(a), we depict a generic SAR dataset made of ten acquisitions that we couple in interferometric pairs by applying the Delaunay triangulation method [see Fig. 3(b)]. Now, let us consider a PhU error that affects one of the interferograms internal to the network, i.e., the interferometric pair belongs to two different triangles [red arc in Fig. 3(c)]. In this case, RIC becomes too large, and the RIP condition is not met. As an example [see Fig. 3(c)], we can easily retrieve that, when we have one PhU error in an internal interferogram, $\|\varepsilon\|_2^2 = 1$; $\|\boldsymbol{C}\varepsilon\|_2^2 = 2 \Longrightarrow \mu = 2$; and similar results $(\mu \geq 2)$ can be found with combinations of errors occurring in internal interferograms with no more than one error for each triangle. Contrarily, when the PhU errors occur only in the interferograms belonging to the network borders [see Fig. 3(d)] (namely, external interferograms), i.e., interferometric pairs that belong to the borders of the network and the corresponding arcs are part of one triangle only, $\|\varepsilon\|_2^2 = \|\boldsymbol{C}\varepsilon\|_2^2 = 1 \Longrightarrow \mu = 1$; it can be easily verified that a similar result $(\mu = 1)$ is always achieved when a number of PhU errors affects external interferograms only.

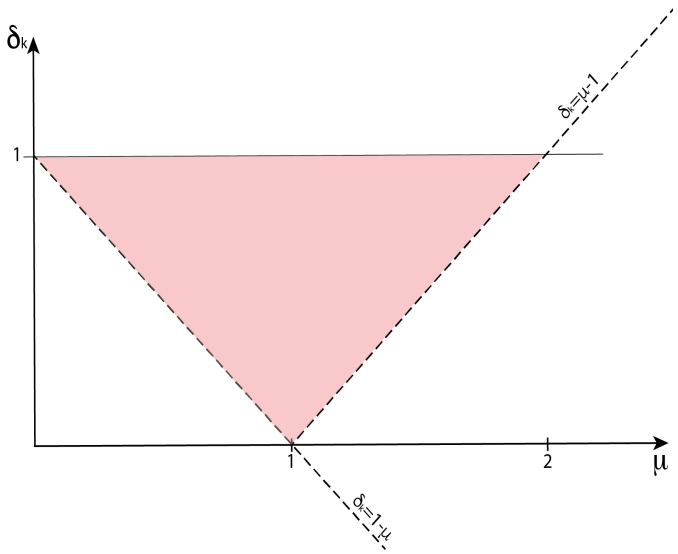

Fig. 2. Graphical representation of (18), whose solution is represented by the red area enclosed by the three lines.

However, a more complex PhU errors distribution [red arcs in Fig. 3(e)] shows that, when PhU errors affect only internal interferograms, a small enough RIC can be achieved; in this case, since in one of the three triangles impacted by the PhU errors the residual is zero, we achieve $\|\varepsilon\|_2^2 = \|\boldsymbol{C}\varepsilon\|_2^2 = 2 \Longrightarrow \mu = 1$. Finally, let us now consider a simple combination of internal and external PhU errors [see Fig. 3(f)]; in this latter case, we have $\|\varepsilon\|_2^2 = 3$; $\|\boldsymbol{C}\varepsilon\|_2^2 = 1 \Longrightarrow \mu = 1/3$, corresponding to $\delta_k \geq (2/3)$, which guarantees robust solution through the CS approach.

These simple examples demonstrate that the C matrix does not satisfy the RIP condition, i.e., a value of $\delta_k \in (0, 1)$ such that (8) is satisfied for any u vector does not exist, even if we consider only very sparse PhU errors ($k = 1$). However, the value of δ_k is strongly impacted by the distribution of PhU errors in the several triangles of the network, and in a large number of cases, we have a high probability to have a small enough RIC, as happens in a large number of real applications where CS is successfully used and good results are achieved even though RIP condition is not satisfied [53]. However, to achieve more robust solutions, we properly adapt the L_1 estimation algorithm to take into account the characteristics of the processed DInSAR dataset; moreover, in order to assess the results of the CS procedure, we introduce a quality function that allows us to recognize and discard unreliable results.

In order to estimate and compensate for possible PhU errors, we implement a solution of (16) by benefitting from the iterative reweighted least-squares (IRLS) method proposed in [54]. The IRLS method is an algorithm largely used to solve L_1 problems by using the L_2-norm solution iterated with a weight function. Generally speaking, in the IRLS method at the n-th step of the iteration process, the solution ε_n of (16) is provided by

$$\varepsilon_n = \left[\boldsymbol{W}^T\boldsymbol{W}\right]^{-1}\boldsymbol{C}^T\left[\boldsymbol{C}\left[\boldsymbol{W}^T\boldsymbol{W}\right]^{-1}\boldsymbol{C}^T\right]^{-1}\boldsymbol{\phi}^{tr} \tag{19}$$

where W is a diagonal weight matrix defined as follows:

$$\boldsymbol{W} = \text{diag}(\text{abs}(\varepsilon_{n-1})^{1/2}). \tag{20}$$

The method proposed in [54] slightly modifies this approach to include a homotopy update factor that improves the robustness and convergence performances of the algorithm.

The IRLS method can be applied to a general problem defined by (16) and does not take into account the peculiarities of the specific problem. In particular, we know that very small temporal baseline interferograms are statistically less affected by PhU errors, whereas large deformation signals can significantly increase the number of PhU errors of long temporal interferograms. Accordingly, we modify the IRLS implementation by adapting the procedure to "foster" the correction of long temporal interferograms. In particular, we modify the diagonal weight matrix $\boldsymbol{W}$ by introducing the temporal baseline values of the interferometric pairs, and (20) becomes

$$\boldsymbol{W} = \text{diag}(\text{abs}(\varepsilon_{n-1} * \left(B_{\text{temp}}\right)^{\alpha})^{1/2}) \tag{21}$$

where $B_{\text{temp}} = [B_0, \ldots, B_{M-1}]$ is the vector of the temporal baselines of the interferograms of the Delaunay triangulation, normalized with respect to the maximum temporal baseline value ($0 < |B_i| \leq 1, \forall\ B_i \in B_{\text{temp}}$). α is a parameter that depends on the SAR dataset; we estimate that proper values of α range between 0 and 4 (0 is the original IRLS); high values of α lead to more weighting of long temporal interferograms to the detriment of the shorter ones.

It is worth noting that the proposed algorithm does not retrieve integer numbers, as, instead, it is requested in the PhU operation; accordingly, the final result is rounded to the closest integer

$$\varepsilon_{\text{rnd}} = \text{round}(\varepsilon). \tag{22}$$

To evaluate the quality of the solution and discard those points for which the solution is not acceptable, we apply a double check. First, since we are searching for a sparse vector ε_{rnd}, we consider only solutions, where

$$\|\varepsilon_{\text{rnd}}\|_0 < \text{th}_{\text{sparse}}. \tag{23}$$

As the algorithm estimates sparse PhU error vectors and no model or *a priori* information is used to drive the PhU errors estimation, values of $\text{th}_{\text{sparse}}$ smaller than 10% of M are strongly recommended in order not to violate the sparsity constraint.

The second quality function is based on the capability of the algorithm to find integer solutions, by defining a coherence function as follows:

$$\gamma_{\text{rnd}}(x, r) = \frac{1}{M}\left|\sum_{i=1}^{M} e^{j(\boldsymbol{\varepsilon_{rnd}}(x,r) - \boldsymbol{\varepsilon}(x,r))}\right|. \tag{24}$$

$\gamma_{\text{rnd}}(x, r)$ ranges in the interval [0, 1] and becomes 1 when all the elements of $\boldsymbol{\varepsilon}(x, r)$ are integer numbers; only the points with $\gamma_{\text{rnd}}(x, r) > \text{th}_{\text{rnd}}$ are considered well unwrapped. Very high values of th_{rnd} (greater than 0.9) are recommended.

As a final remark, it is worth noting that other works have already shown the effectiveness of the L_1-norm solution in

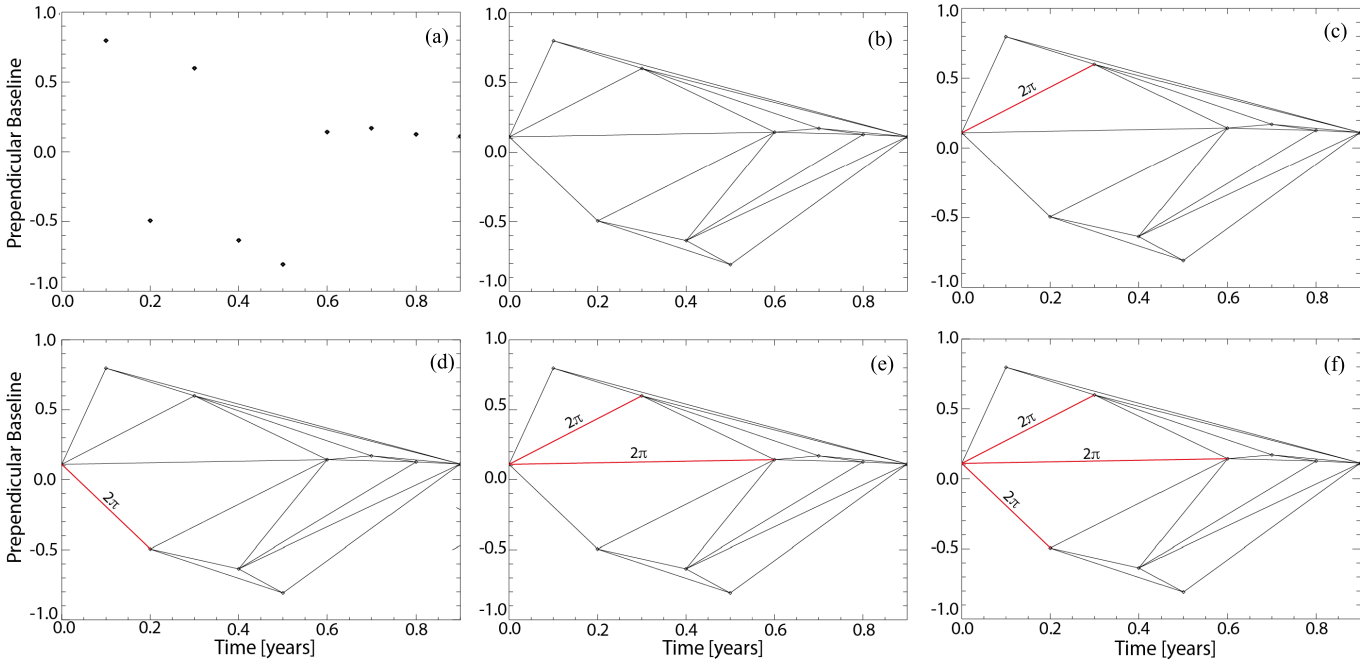

Fig. 3. Simplified example of possible distributions of PhU errors. The SAR dataset is represented in the temporal/spatial baseline plane; each acquisition is represented by a black diamond, whereas the arcs represent the interferometric pairs. (a) Ten SAR acquisitions dataset. (b) Acquisitions are paired using the Delaunay triangulation method to select the interferometric pairs. (c) Single PhU error (red arc) in an internal interferogram. (d) Single PhU error (red arc) in an external interferogram. (e) Two PhU errors (red arcs) in internal interferograms belonging to the same triangle. (f) Three interferograms with PhU errors (red arcs), where two are located inside the network and one is at the outer edge of the network.

mitigating PhU errors. In particular, in [18] and [20], the developed methods benefit from L_1- and *Huber*-norms to mitigate the impact of PhU errors and noise effects in the generation of deformation time series, but no 2π constrain is applied on the corrections. Conversely, in our method, we first estimate and compensate for PhU errors (2π multiples) to correct the unwrapped interferograms, and subsequently, we generate the time series. Moreover, in our method, a Delaunay triangulation in the spatial/temporal baseline plane is generated to benefit from the phase closure property of the interferometric network, whereas the abovementioned works are based on the inversion of the incidence matrix of the oriented graph associated with the interferometric pairs [see (26)], and the solution is obtained in the L_1- and *Huber*-norm senses. Finally, the two algorithms proposed in [18] and [20] do not benefit from the characteristic of the interferometric dataset, whereas the method proposed in this work introduces the temporal baseline factor (weighted by the α parameter) in the procedure to retrieve the optimized L_1-norm solution.

IV. CS-Based PhU Errors Correction in the SBAS Approach

In order to demonstrate the effectiveness of the proposed CS approach and assess its performance, we tailor it to the FR SBAS processing chain. The SBAS algorithm is a two-scale approach that works with multilook and single-look interferograms to carry out regional (low-resolution) and local (high-resolution) analyses of the displacements that occurred in an area of interest [38]–[40], [42]–[44]. The rationale of the SBAS approach is the generation of a stack of small baseline interferograms to reduce the noise effects (decorrelation phenomena) and maximize the number of coherent points that can be detected. Once the wrapped interferometric stack is generated, the interferograms are unwrapped, and subsequently, the time series is retrieved by applying, on a pixel-by-pixel basis, the SVD method. Finally, the atmospheric artifacts are estimated and compensated for in the time series by applying spatial and temporal filterings [7]. We implement the proposed CS method to retrieve and correct the PhU errors in both regional and local scale SBAS processing chains, before applying the SVD method. The detailed description of the two enhanced processing chains is now in order.

A. Regional-Scale SBAS Analysis

A detailed description of the conventional regional-scale SBAS processing chain can be found in [47] and [48]. In this work, we mainly focus on the modifications applied to the conventional chain (see Fig. 4) to estimate and correct the PhU errors with the proposed CS-based algorithm. The red block in Fig. 4, referred to as PhU errors' retrieval, is here introduced to implement the CS-based procedure described in Section III, which enhances the SBAS processing chain.

Let us assume to have an SAR dataset of $N+1$ acquisitions acquired at the ordered times $\boldsymbol{t} = [t_0, t_1, \ldots, t_N]$, from which a list of M small baseline interferometric pairs can be produced; an effective way to select the interferometric pairs has been proposed in [51], where the Delaunay triangulation method, applied in the spatial/temporal baseline plane, is exploited. From the list of small baseline pairs, a low-resolution (multilook) wrapped interferometric stack is produced and then unwrapped, as described in [47] and [48]. The final step of the conventional SBAS approach concerns the generation

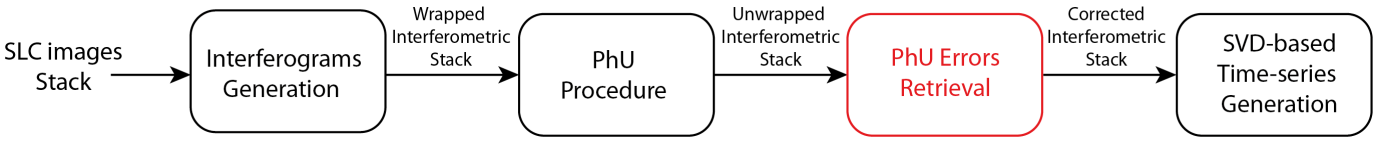

Fig. 4. Schematic block diagram of the CS-based regional-scale SBAS approach. The red box indicates the new processing step that implements the CS procedure developed to mitigate the PhU errors, whereas the black boxes belong to the conventional regional-scale SBAS processing chain.

of deformation time series, by searching for the minimum norm least-squares solution through the exploitation of the SVD method, and the estimation of the DEM errors and the atmospheric phase screen component.

In the CS regional-scale SBAS processing chain, we introduce a new processing step (red block in Fig. 4), based on the CS procedure described in Section III, to estimate and compensate for possible PhU errors. The new processing step works with the stack of spatially unwrapped interferograms; the developed algorithm can be applied to interferograms unwrapped with any method, such as those proposed in [51] and [55], and the only requirement concerns the selection of the interferometric pairs that has to be based on a triangulated network. The proposed procedure deals with a pixel-by-pixel analysis, i.e., all pixels are analyzed independently of each other, which allows the pixels to be computed in parallel, so the developed algorithm is intrinsically suitable to be implemented by benefitting from parallel programming techniques to reduce its computing time.

Once the 2π multiples are retrieved and corrected, only the points that have $\gamma_{\text{rnd}} > \text{th}_{\text{rnd}}$ and $\|\varepsilon_{\text{rnd}}\|_0 < \text{th}_{\text{sparse}}$ [see (23) and (24)] are selected, and the processing can then move on to the SVD-based module and the reconstruction of the deformation time series.

B. Local-Scale SBAS Analysis

The local-scale SBAS approach is properly modified to introduce the PhU error retrieval procedure. To better understand how such an SBAS chain is enhanced, we quickly summarize the main steps of the approach. Benefitting from the list of M small baseline interferometric pairs, selected by using the method described in [51], a wrapped FR interferometric stack is generated. The FR stack (single-look), together with the low-pass (multilook) products, represents the input of the high-resolution SBAS approach (see Fig. 5).

The first step of the chain is the HP filter; the low-pass products are removed from the FR interferograms by carrying out a modulo-2π subtraction; the HP residual phase is retrieved; and the m_{th} interferogram, for each point with azimuth and range coordinates (x, r), can be expressed as follows[2]:

$$\delta\phi_m^{\text{HP}}(x,r) = \frac{4\pi}{\lambda}\left[\left(t_{\text{IE}_m} - t_{\text{IS}_m}\right)v^{\text{HP}}(x,r) + \beta\left(t_{\text{IE}_m},x,r\right) - \beta\left(t_{\text{IS}_m},x,r\right) + \frac{b_m \Delta z^{\text{HP}}(x,r)}{r\sin(\theta)}\right] + \Delta n_m^{\text{HP}}(x,r) \tag{25}$$

[2]Note that our analysis is based on [5] for the sake of simplicity. A more complex and realistic expression, proposed by Bonano *et al.* [33], can be easily taken into account without any change of the general meaning.

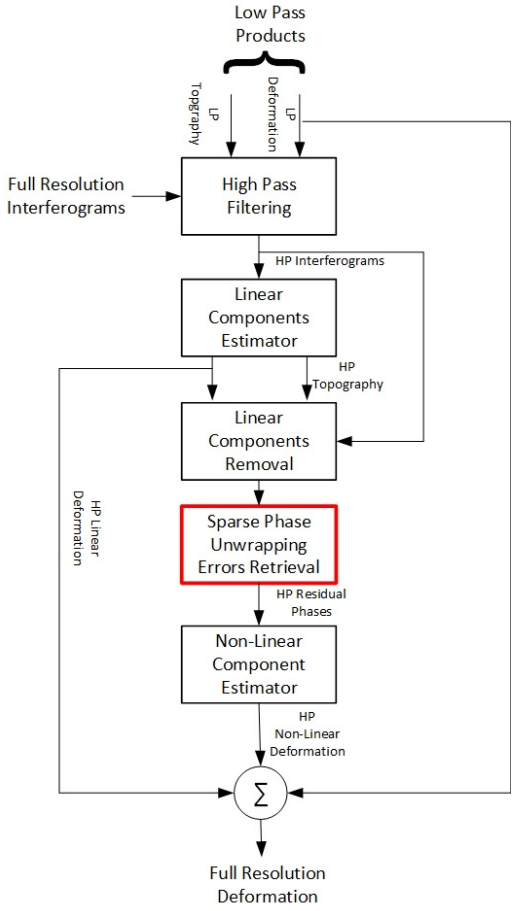

Fig. 5. Block diagram of the local-scale SBAS processing chain enhanced with the CS-based PhU error correction algorithm (red block).

where t_{IE_m} and t_{IS_m} represent the acquisition time of the slave and master images, v^{HP} and β represent the HP linear and nonlinear components of the residual displacement, Δz^{HP} is the residual topography, and Δn_m^{HP} is the noise term, whereas b_m and θ are the perpendicular component of the spatial baseline and the incidence angle, respectively.

The expression in (25) is solved pixel-by-pixel by applying a two-step approach; first, the linear components of v^{HP} and Δz^{HP} are estimated by maximizing the linear model coherence factor [5]. Subsequently, the nonlinear deformation component β is computed by solving the following linear system with the SVD method:

$$\boldsymbol{A} \cdot \beta = \delta\phi^{\text{res}} \tag{26}$$

where $\boldsymbol{A}$ is the incidence matrix of the oriented graph associated with the interferometric pairs in the spatial/temporal baseline plane (start and end points of each arc are the master

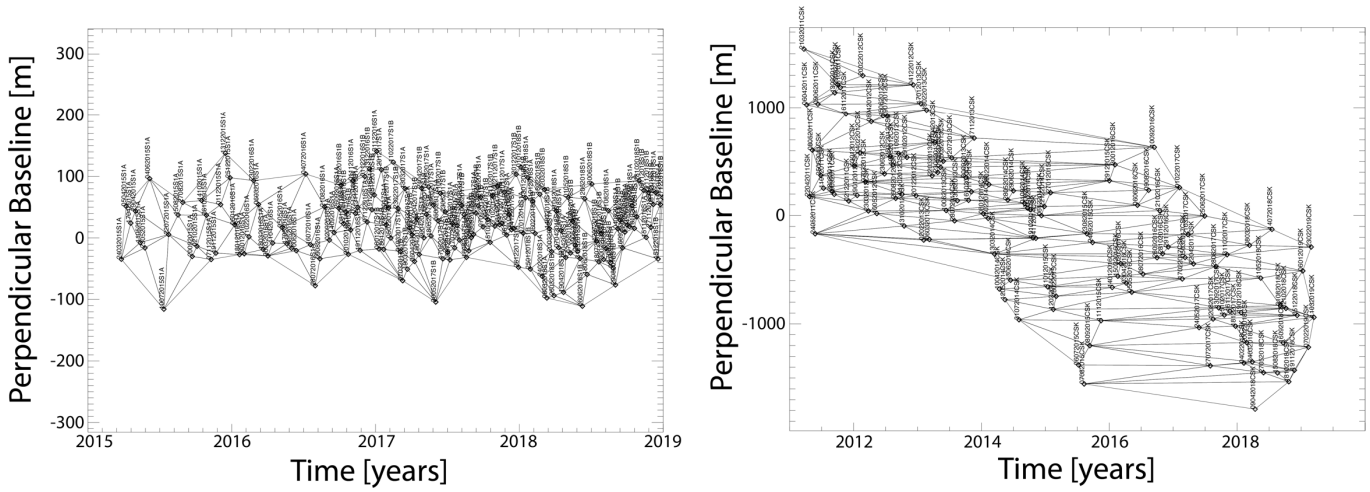

Fig. 6. Distribution of (Left) Sentinel-1 and (Right) COSMO-SkyMed acquisitions used in the experimental analyses. Each acquisition is represented by a black diamond, with the date of acquisition as the code name of the image, whereas the arcs represent the selected interferometric pairs. The complete list of images and interferometric pairs is reported in the supplementary material.

and slave images of each interferometric pair, respectively), and $\beta = [\beta_0, \beta_1, \ldots, \beta_N]$ is the vector of the $N+1$ nonlinear phase components. $\delta\phi^{\text{res}} = [\delta\phi_0^{\text{res}}, \ldots, \delta\phi_{M-1}^{\text{res}}]$ is the vector of the M interferometric residual phases given by, for the generic m_{th} interferometric pair,

$$\delta\phi_m^{\text{res}}(x,r) = \left\langle \delta\phi_m^{\text{HP}}(x,y) - \frac{4\pi}{\lambda}\frac{b_m \Delta z^{\text{HP}}(x,y)}{r\sin(\theta)} - \frac{4\pi}{\lambda}(t_{\text{IE}_m} - t_{\text{IS}_m})v^{\text{HP}}(x,y) \right\rangle_{2\pi} \quad (27)$$

where $\langle * \rangle_{2\pi}$ represents the wrapping operation.

Once the vector β of the nonlinear phases is retrieved, this latter is added, together with the HP mean deformation velocity v^{HP}, to the regional-scale deformation time series to achieve the full-resolution time series. A similar operation is carried out on the low-pass and HP topography components. It is worth noting that (27) is computed in the wrapped form; however, the resulting $\delta\phi^{\text{res}}$ component can often be considered unwrapped in the $[-\pi, +\pi)$ interval and solved according to (26) without any additional unwrapping operation.

In order to improve this latter step and filter out the possible PhU errors that may impact on $\delta\phi^{\text{res}}$ phase term, i.e., to properly solve those cases when some elements of $\delta\phi^{\text{res}}$ are not unwrapped, we implement the PhU errors' retrieval procedure describe in Section III. As for the approach implemented in the regional-scale processing chain, we modify the conventional local-scale SBAS algorithm by introducing a new step that estimates and correct the possible PhU errors of the HP residual phase $\delta\phi^{\text{res}}$ (red block in Fig. 5) before applying the SVD module. In particular, once the residual phase $\delta\phi^{\text{res}}$ is retrieved, we can reasonably assume that: 1) the PhU errors are sparse with respect to the number M of interferometric pairs and 2) they mainly affect long temporal interferograms due to important nonlinear displacement signals. Accordingly, possible PhU errors can be effectively retrieved and compensated for by applying the procedure described in Section III. The correction of PhU errors is carried out on a pixel-by-pixel basis and can be applied to all or only a subset of pixels to reduce the processing time.

V. Experimental Results

In order to investigate the performance of the developed algorithm and assess its capability in recovering PhU errors, we carry out an experimental analysis based on simulated and real data. In particular, we select a Sentinel-1 (S-1) dataset acquired between March 2015 and December 2018 over Central Italy from descending orbits (track number 22). The S-1 dataset is made of 171 acquisitions that are paired in 478 interferograms.

Moreover, we also use a CSK ascending dataset acquired over the city of Rome between March 2011 and March 2019. The CSK dataset consists of 129 Stripmap SAR images paired in 361 interferograms.

The two interferometric networks are shown in Fig. 6; the lists of the used images and selected interferometric pairs are provided in the Supplementary Material.

A. Simulated Data

To carry out the experimental analysis on simulated data, we use the S-1 dataset acquired over Central Italy, and we select a number of simulated signals (see Fig. 7) from which the unwrapped interferometric phases are retrieved; these phases are then wrapped to simulate PhU errors. By wrapping the interferometric phases, we are simulating the worst case we could address, i.e., when the PhU procedure totally fails and no 2π multiple is retrieved. The number, magnitude, and positions of PhU errors are shown in the second column of Fig. 7, whereas the least-squares solution is depicted in the third one. The magnitude of the signals is set up to have a number of PhU errors large enough to be a representative test case but with a maximum number of uncorrected interferograms that do not exceed 10% of the total number of interferograms to guarantee the solution sparsity. In particular, we simulate

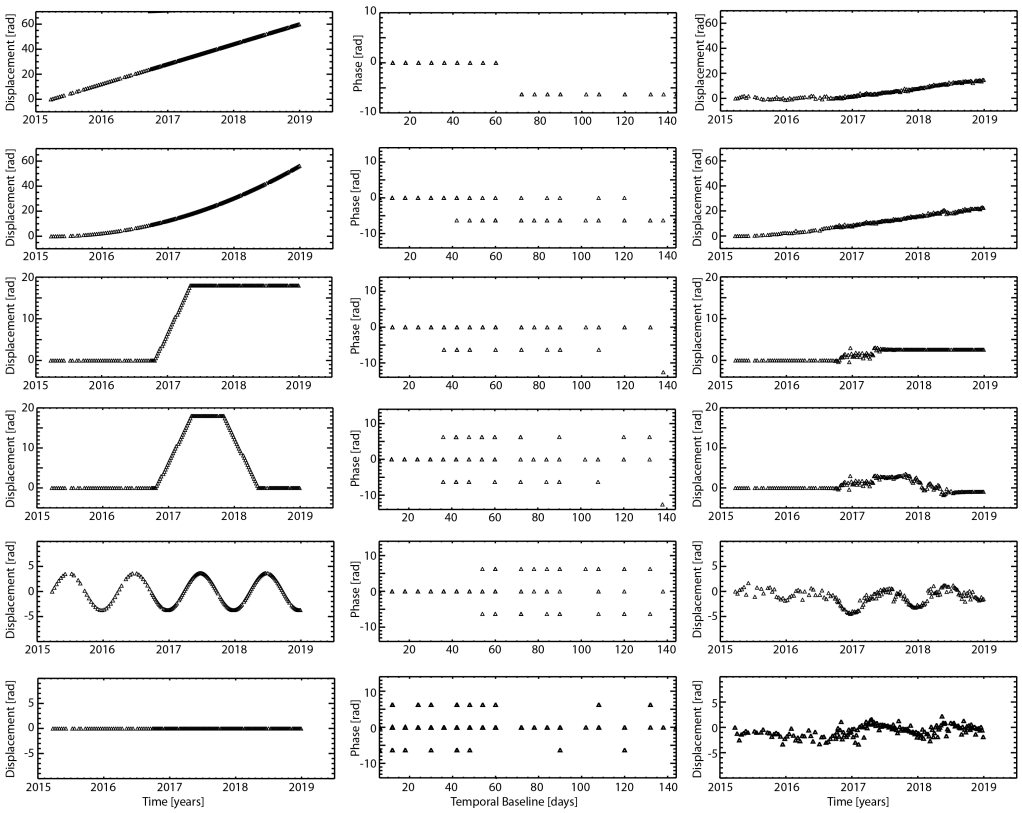

Fig. 7. Simulated dataset. The original simulated signal is reported on the left column, whereas, in the second one, the PhU errors in the interferograms, ordered for increasing values of temporal baseline, are shown. The column on the right represents the solution retrieved by using the minimum L_2-norm criterion.

displacement phenomena with linear and parabolic behaviors with a maximum amplitude of 60 rad in the analyzed time period, single- and double-step functions with a maximum amplitude of 18 rad, a one-year periodic function with an amplitude of 4 rad, and a constant signal. Different from the others, in the last example (constant signal), we add uniformly distributed PhU errors to simulate random errors, i.e., in this latter case, the PhU errors do not affect mainly long temporal interferograms, but each interferometric pair has the same probability to have errors of 2π multiplies. The number of PhU errors for each of the simulated signals is between 40 and 50, except for the one-step behavior where it is smaller than 30. As easily foreseeable, due to the large numbers of 2π errors, in all the simulations, the least-squares solution is significantly distant from the original signal (third column in Fig. 7).

The results obtained by applying the proposed CS-based technique are shown in Fig. 8. For each signal, we apply four different values of the α parameter pointed out in (21) (0, 1, 2, and 4 from left to right columns in Fig. 8, respectively). In each time series of Fig. 8, the retrieved L_1 result is represented with red triangles, whereas the continuous black line is the original signal; for each time series, the standard deviation value σ of the difference between the original and the retrieved signals is reported. For the first five signals, it is evident that the quality of the result gets better as α increases, becoming very good for $\alpha = 2$ and excellent for $\alpha = 4$, whereas the last example shows that, when the errors are randomly distributed with respect to the temporal baseline values of the interferometric pairs, the best results are achieved for low values of α. This is further confirmed by computing the average standard deviation between the six results of Fig. 8 for each value of α (3.83, 2.93, 1.13, and 0.57 rad for α from 0 to 4, respectively). Accordingly, in the following analyses, the value of the parameter α will be set up equal to 2 for better compensating the performance of the L_1 estimator with respect to the possible distributions of the PhU errors.

Finally, the performance of the developed method is compared to that of the approaches proposed in [18] and [20] based on the L_1- and *Huber*-norm, respectively. In particular, for the six signals shown in Fig. 7, Fig. 9 reports the results obtained by applying our method with $\alpha = 2$ (red line in Fig. 9), and Lauknes' and Khwaja's approaches (blue and green lines in Fig. 9). It is evident, as in five cases out of six cases, the best reconstruction of the original signal (black line) is provided by our approach, and only in the bottom-right example (random errors), Lauknes' and Khwaja's methods show a smaller number of errors. This comparison points out, once again, the great capability and effectiveness of our technique in reconstructing strongly nonlinear deformation signals.

B. Regional-Scale SBAS Results

To assess the performance of the CS-enhanced regional-scale SBAS chain, we carry out an experimental analysis on real SAR data acquired by the Sentinel-1 constellation over Central Italy (see Fig. 10), as shown

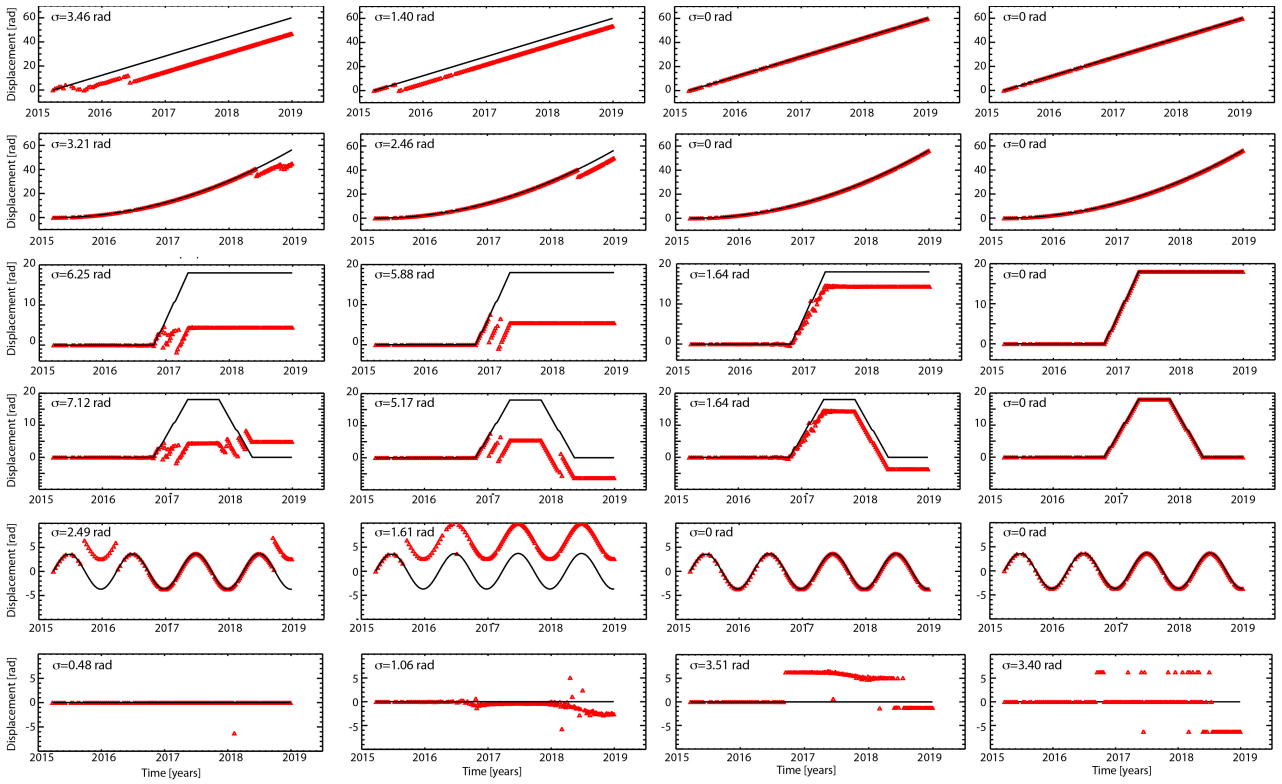

Fig. 8. Experimental results of the developed CS-based method achieved with the simulated dataset. The black solid line is the original simulated signal; red triangles represent the retrieved minimum L_1-norm solution. (Left to Right) Columns show the results with $\alpha = 0, 1, 2$, and 4, respectively. For each time series, the standard deviation (σ) between the original and the retrieved signal is reported.

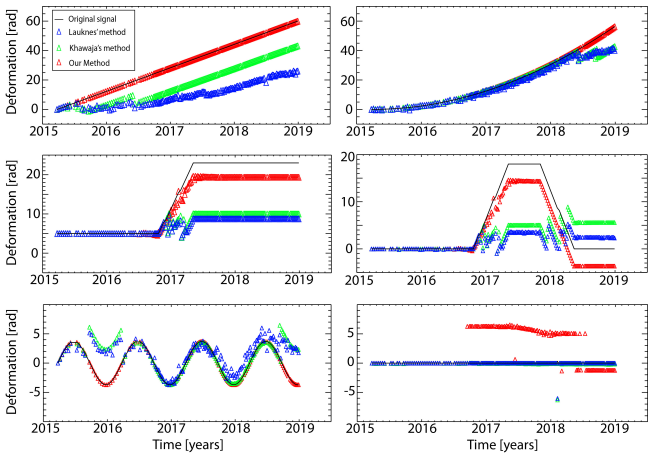

Fig. 9. Comparison between the performance of our method (red line) and the L_1-norm (blue line) and *Huber*-norm (green line) approaches proposed in [18] and [20], respectively. The original signals are those depicted in Fig. 7, here represented with the black line.

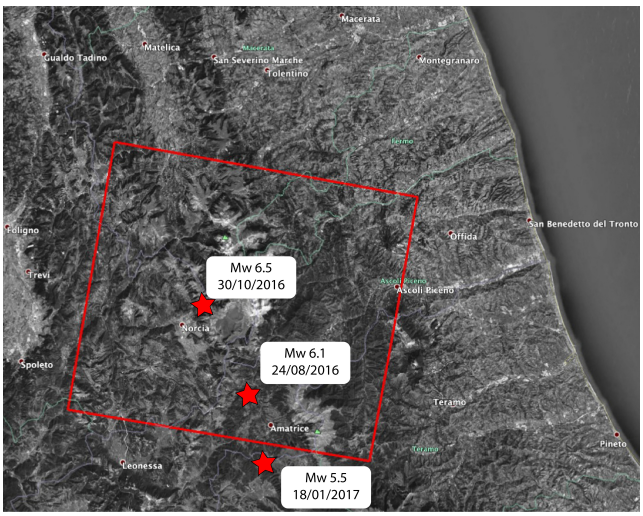

Fig. 10. Red: footprint of the Sentinel-1 dataset over Central Italy. Red stars: epicenters of the three main earthquakes that occurred in the area between 2016 and 2017.

in Fig. 6. The analyzed area is around 50 × 50 km and was affected between 2016 and 2017 by a long seismic sequence, characterized by three main shocks that occurred on August 24, 2016 (Amatrice earthquake), October 30, 2016 (Norcia-Visso earthquake),[3] and January 18, 2017 (Montereale earthquake); the magnitude and the location of the epicenters of the three main shocks are reported in Fig. 10. To carry out the assessment of the results achieved with the developed CS algorithm, we perform a comparison with those obtained with the conventional regional-scale SBAS chain. It is worth noting that the selection of the coherent points in the SBAS analysis is based on the temporal coherence

[3]The two main earthquakes, occurred on October 26 and 30, 2016, cannot be distinguished with the used S-1 dataset because no SAR scene was acquired between the two events. Accordingly, throughout this article, they will be considered as a unique event.

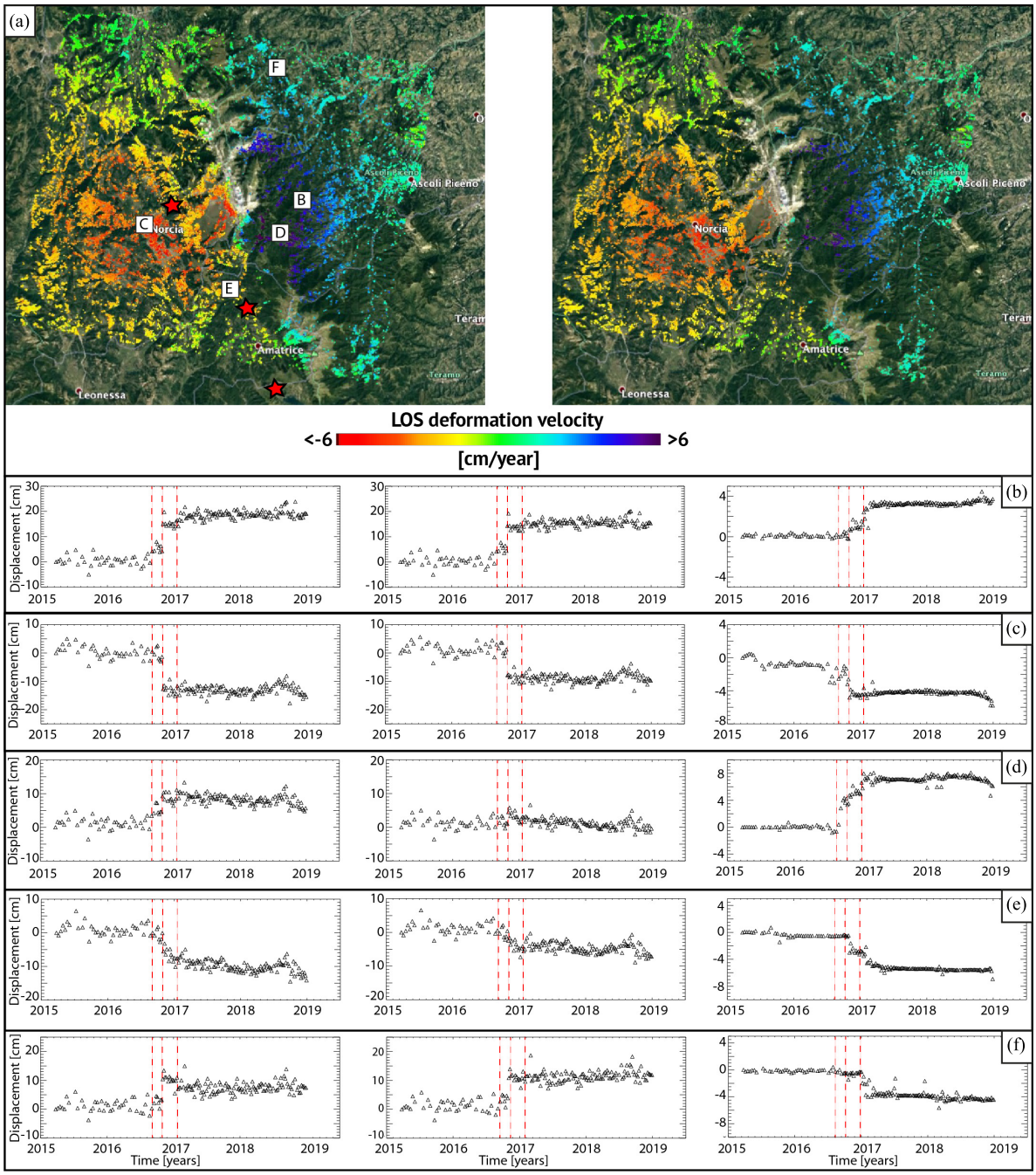

Fig. 11. (a) LOS mean deformation velocity maps generated through (Left Top) CS-based and (Right Top) conventional regional-scale SBAS processing chains. (b)–(f) Comparisons between the deformation time series estimated by (Left) CS-based and (Middle) conventional regional-scale analyses for five points whose location is pointed out in (a). The third column is relevant to the difference between the two SBAS time series. The dashed red lines reported in each plot are relevant to the occurrences of the three main shocks (Amatrice, Norcia-Visso, and Montereale) registered in the analyzed area.

function γ_{tp}[51]

$$\gamma_{\text{tp}} = \frac{\left|\sum_{i=1}^{M} e^{j(\Delta\varphi_i - \Delta\hat{\varphi}_i)}\right|}{M} \tag{28}$$

where M is the number of the interferometric pairs; $\Delta\varphi_i$ and $\widehat{\Delta\varphi_i}$ represent the wrapped (original) and unwrapped (estimated) phases of the i_{th} interferogram, respectively; the unwrapped phase $\widehat{\Delta\varphi_i}$ is regenerated from the time series retrieved with the SVD-based module (see Fig. 4). Note that, for pixels where $\gamma_{\text{tp}} \to 1$, we expect that no unwrapping error is present, as a quasi-perfect retrieval of the original phase has been obtained.

To assess the performance of the CS-based algorithm, we first investigate the coherent point density. In both analyses, the coherent points are selected by using a threshold of 0.85 for the temporal coherence in (28). For the CS-based SBAS analysis, in addition to the temporal coherence criterion, we also use (23) and (24). In particular, we set up $\text{th}_{\text{sparse}} = 30$, corresponding to around 6% of the number of interferograms,

and $th_{rnd} = 0.95$. The CS-based SBAS approach achieves an improvement of around 40% of points with respect to the conventional one (31 053 points the former and 22 070 points the latter); such an outcome represents the first evidence of the impact of the mitigated PhU errors.

The capability of the CS algorithm to mitigate PhU errors and retrieve a larger number of coherent points is evident and even more relevant if we consider the location of the denser areas. Fig. 11(a) shows the two geocoded mean deformation velocity maps superimposed on an optical image of the area; the zones mainly interested by the increase of coherent points are placed where the maximum displacement magnitudes are estimated, along the major active faults that generated the seismic sequence occurred between 2016 and 2017 [56], [57]. This result demonstrates that the proposed algorithm can significantly improve the quality of the SBAS results when large and significantly nonlinear deformation signals occur. To better explain this point, in Fig. 11(b)–(f), we show the line-of-sight (LOS) deformation time series, retrieved with CS (left) and conventional (central column) regional-scale SBAS chains (whereas the last column on the right reports their difference) in some relevant areas affected by seismic movements.[4] The atmospheric phase screen is not filtered out in the LOS time series shown in Fig. 11(b)–(f) not to tamper the analysis on the impact of the detected PhU errors with the effects of any postprocessing filter. The first two LOS deformation time series [see Fig. 11(b) and (c)] are relevant to two pixels located in the maximum and minimum deformation areas, respectively. In both cases, the CS-based SBAS approach retrieved a deformation signal stronger of about 4 cm, which, in the first case [see Fig. 11(b)], are mainly related to the Montereale earthquake (about 3 cm out of 4), whereas, in the second time series, most of PhU errors mainly impact on the October 30 event (Norcia-Visso earthquake).

Let us now consider the pixel D located in the neighbor of the town of Arquata del Tronto; we show a point where conventional SBAS chain does not estimate the seismic pattern, whereas the CS-enhanced analysis correctly detects the deformation resulting from the seismic sequence, around 10 cm in LOS. By analyzing pixel E, selected in the surroundings of Amatrice, we note that the deformation time series retrieved with both CS and conventional SBAS chains follows the same trend, but with different dynamics. In particular, while the two results retrieve the same result for the Amatrice earthquake, the developed CS approach detected a larger LOS down lift of around 3 cm related to the Norcia-Visso earthquake and other 2–3 cm in correspondence of the Montereale event.

Finally, the pixels far away from the epicenters (in the Northern zone of the analyzed area) are less prone to deformation, as pixel F in Fig. 11. Both CS and conventional SBAS analyses detect an uplift of around 11 cm, mainly as a result of the Norcia-Visso earthquake; however, the CS approach detected an LOS down lift of around 4 cm related to the Montereale earthquake, which is not revealed in the results of conventional SBAS chain. Since the pixel F is quite far from the epicenter of the last seismic event (Montereale), the deformation time series retrieved with the CS-based analysis could be interpreted as affected by any error. To investigate, more in detail, this latter result, assess its correctness or, eventually, identify possible error sources, we further analyze the area in the surroundings of pixel F.

[4]It is worth noting that the five selected points are not coherent in the conventional SBAS analysis due to the large number of PhU errors.

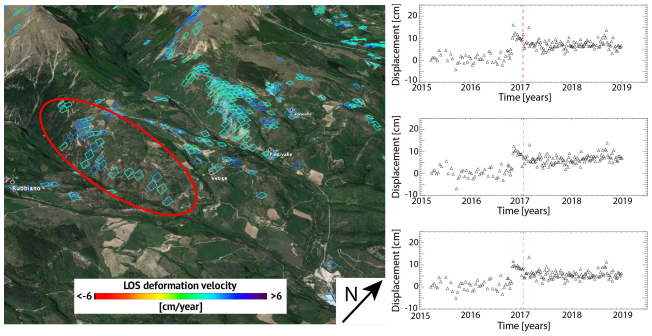

Fig. 12. 3-D Zoomed-in view of the area identified with Fin Fig. 12(a). LOS mean deformation velocity map (left), generated through the CS-based SBAS processing chain, and some deformation time series (right) relevant to pixels located in the area highlighted by the red circle. Although the large distance of this area from the epicenter of the earthquake occurred on January 18, 2017 (Montereale), the pixels located in such an area show a small signal in correspondence to this latter event, probably related to a seismic-induced effect.

In Fig. 12, we show a 3-D view of the area where pixel F is located (the red ellipse in Fig. 12 represents the area under observation). First, we note that this zone is placed along a slope and could be interested in mass movements. Second, other pixels belonging to the same flank show a pattern similar to that shown by pixel F, characterized by a jump in the LOS deformation time series in correspondence with the Montereale earthquake (see the LOS displacement time series in Fig. 12). It is evident that all the time series belonging to the same flank are characterized by a similar pattern. It is worth noting that, in the CS module developed to correct PhU errors, the pixels are analyzed independently of each other; therefore, the spatial consistency of the results may be considered as an indirect assessment of their correctness. Accordingly, the CS-based SBAS chain could have revealed a signal not directly generated by the fault movement of the seismic event (in this case, the jump would be present in a larger area and not only along some slopes) but, more likely, the effect of a possible seismic-induced landslide.

As a final analysis, to assess the accuracy of the deformation signals retrieved with the CS-based SBAS chain, we focus on the deformation pattern generated by the Norcia-Visso earthquake (October 30, 2016), which is the strongest seismic event that occurred in this area during the analyzed period. This event has been widely investigated by also using InSAR methods [57]; therefore, we can use it as a test case for the assessment of the accuracy of the proposed algorithm. In Fig. 13(a), we show the displacement map retrieved by unwrapping the differential interferogram related to the October 26 and November 1, 2016, S-1 images. This interferometric pair has the shortest temporal baseline among the possible pairs covering the event, and it allows us to accurately reconstruct the deformation pattern related to the

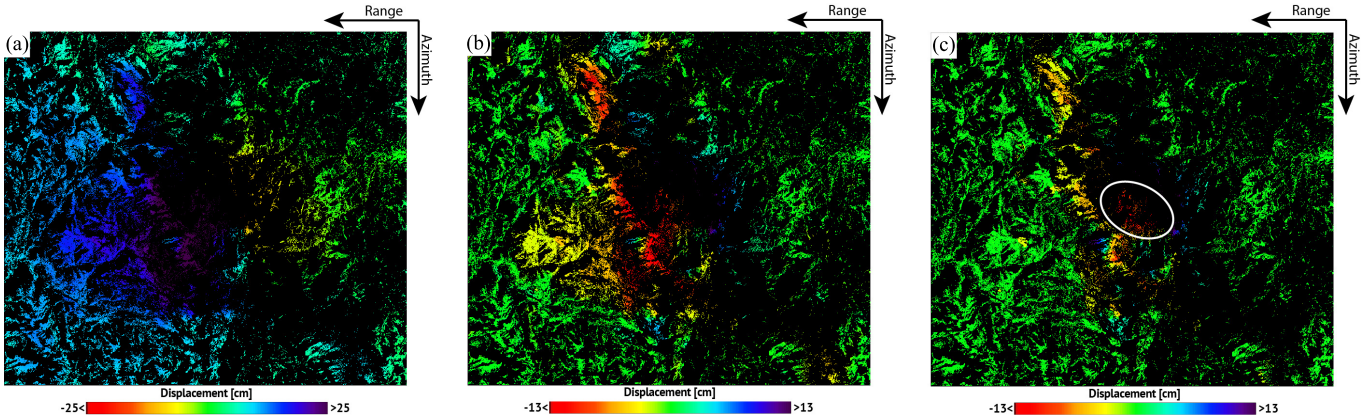

Fig. 13. (a) Displacement map retrieved by unwrapping the differential interferogram generated processing the two S1 images acquired on October 26 and November 1, 2016. (b) Difference between the map shown in Fig. 13A and the corresponding map extracted by the conventional SBAS time series. (c) Difference between the map shown in (a) and the corresponding map extracted by the CS-based SBAS time series. The white circle in (c) represents the area of maximum deformation.

Fig. 14. Optical image of the city of Rome. The area analyzed with the CSK dataset (about 6×4 km^2) is highlighted by the red rectangular box; the area includes part of the downtown, some famous Roman archeological sites, and the southern part of the city interested in significant deformation phenomena.

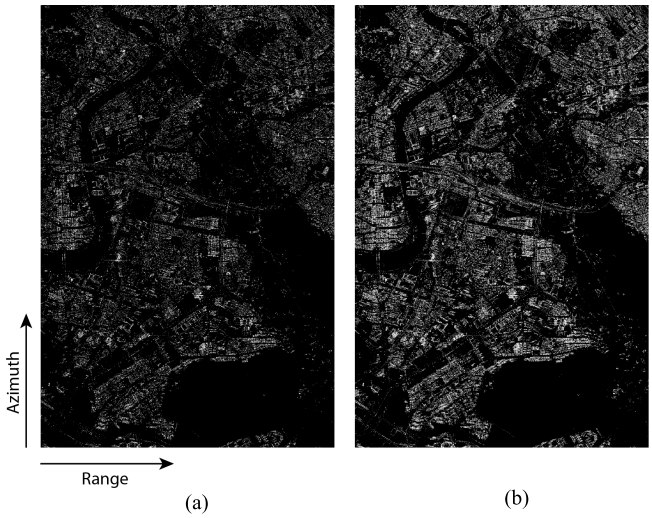

Fig. 15. Coherence maps relevant to the city of Rome were achieved with (a) conventional and (b) CS-based local-scale SBAS analyses.

Norcia-Visso earthquake. The deformation map is retrieved by applying the Minimum Cost Flow unwrapping approach described in [55], and the displacement results are in perfect agreement with those presented in other geophysical studies related to such a seismic event [57]. In Fig. 13(b) and (c), we show the difference (residual) between the displacement map of Fig. 13(a) and the corresponding signals achieved with the conventional and CS-based SBAS chains, respectively. The impact of the PhU errors mitigation operation is evident from the visual comparison of Fig. 13(b) and (c); indeed, the deformation pattern is more accurate after the compensation of PhU errors estimated with our method [the residuals in Fig 13(c) are significantly smaller than those in Fig. 13(b)], and only the area of maximum deformation still shows an underestimated pattern [white circle in Fig. 13(c)]. To provide a quantitative analysis of the retrieved results, we compute the standard deviation of the residuals presented in Fig. 13(b) and (c), and we achieve about 2.5 cm for the conventional SBAS results and 1.5 cm for those corrected with the proposed approach, thus demonstrating the effectiveness of our approach in mitigating PhU errors in the presence of strongly nonlinear deformation patterns.

C. Local-Scale SBAS Results

To assess the performance of the CS-enhanced SBAS approach at the local scale, we use an FR SAR dataset composed of 129 scenes paired in 361 interferograms (see Fig. 6) acquired by the CSK constellation between 2011 and 2019 over the city of Rome from ascending orbits. In particular, we process an area of about 6 km $\times$ 4 km around the downtown city of Rome (see Fig. 14). This area includes the

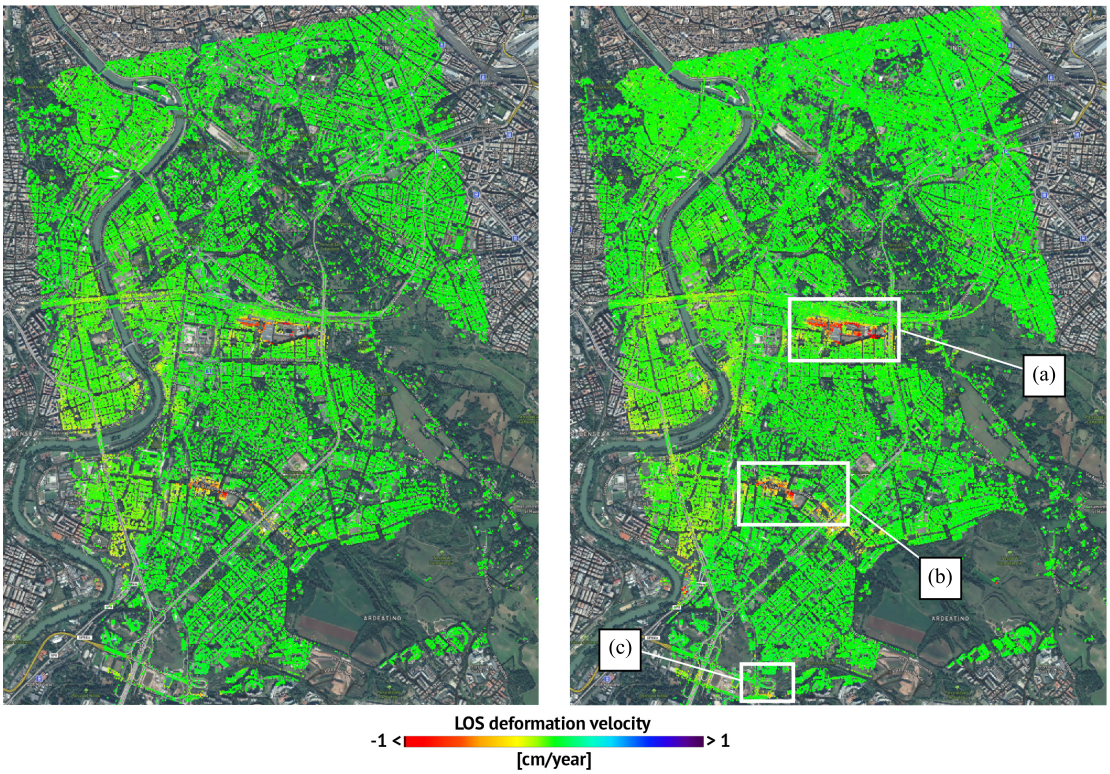

Fig. 16. LOS mean deformation velocity maps relevant to (Left) conventional and (Right) CS-enhanced SBAS chains, superimposed on an optical image of the area of interest. The three rectangular boxes, referred to as (a)–(c), represent the Ostiense Station, Via Giustiniano Imperatore, and a public park, respectively. The three selected areas are characterized by relevant deformation phenomena.

most ancient zone of the city, where some world-renowned Roman ruins are present (e.g., Colosseum, Palatino Hill, Foro Romano, Foro Traiano, Domus Aurea, and Circo Massimo), and the southern part of the city, where well-known deformation phenomena (e.g., Ostiense Station and Via Giustiniano Imperatore) were deeply analyzed by using multitemporal DInSAR techniques [40], [43], [58]–[60].

In order to assess the results achieved with the CS FR SBAS approach, we compare the new results with those achieved with the conventional FR SBAS processing chain. The two analyses (conventional and CS-based) are carried out only on pixels with a model coherence factor (see (25) and [5]) greater than 0.25, in order to speed up the processing time by discarding points significantly affected by decorrelation effects; accordingly, around 25% of the SAR pixels are processed (1 538 109 pixels out of 6 000 000).

A direct comparison of the results of the two SBAS analyses is first based on the number of the retrieved coherent points. Fig. 15 shows the distribution of coherent points of conventional (left) and CS-based (right) SBAS processing retrieved over the analyzed area.

To compare the results achieved with the two chains, we select the coherent points with homogenous criteria. In particular, in both analyses, the coherent points are selected by using the temporal coherence criterion (28) with a threshold of 0.85 and 0.95 for the conventional and CS-based analyses, respectively. Moreover, in the CS-based SBAS processing, we also apply (23) and (24) with 20 (5.5% of the number of interferometric pairs) and 0.95 thresholds, respectively. It is worth noting that, in the case of the CS-enhanced SBAS approach, the temporal coherence value can be set up to a value significantly higher than the conventional one due to the reduced number of PhU errors that allow us to be more restrained on the acceptable noise level of the time series. Indeed, despite the more prudent thresholds applied in the CS FR processing, the number of coherent points is significantly larger, as it is quite evident in Fig. 15, with an increase of about 85% (381 609 points retrieved in the conventional SBAS approach and 708 614 with the CS-based one).

To better analyze such an improvement, in Fig. 16, the two mean deformation velocity maps are represented in geographic coordinates and superimposed on an optical image of the area. It is evident that the increase in the number of coherent points achieved with the CS approach concerns the whole area, and it allows us to better map the ongoing deformation phenomena. To show this, we select three zones, referred to as (a), (b), and (c) in Fig. 16, where relevant deformation signals are detected. The zoomed-in view of these three areas is shown in Fig. 17, where the CS-based results are shown on the left and the conventional ones on the right. In particular, Fig. 17(a) and (b) shows the Ostiense Station and Via Giustiniano Imperatore, respectively, where deformation phenomena related to soil compaction are still ongoing [58], [59], and Fig. 17(c) is relevant to a public park located in the southern part of the investigated area.

Through the visual inspection of Fig. 17, we note that the results achieved with the CS approach allow us to recognize spatial details about the ongoing phenomena that are not

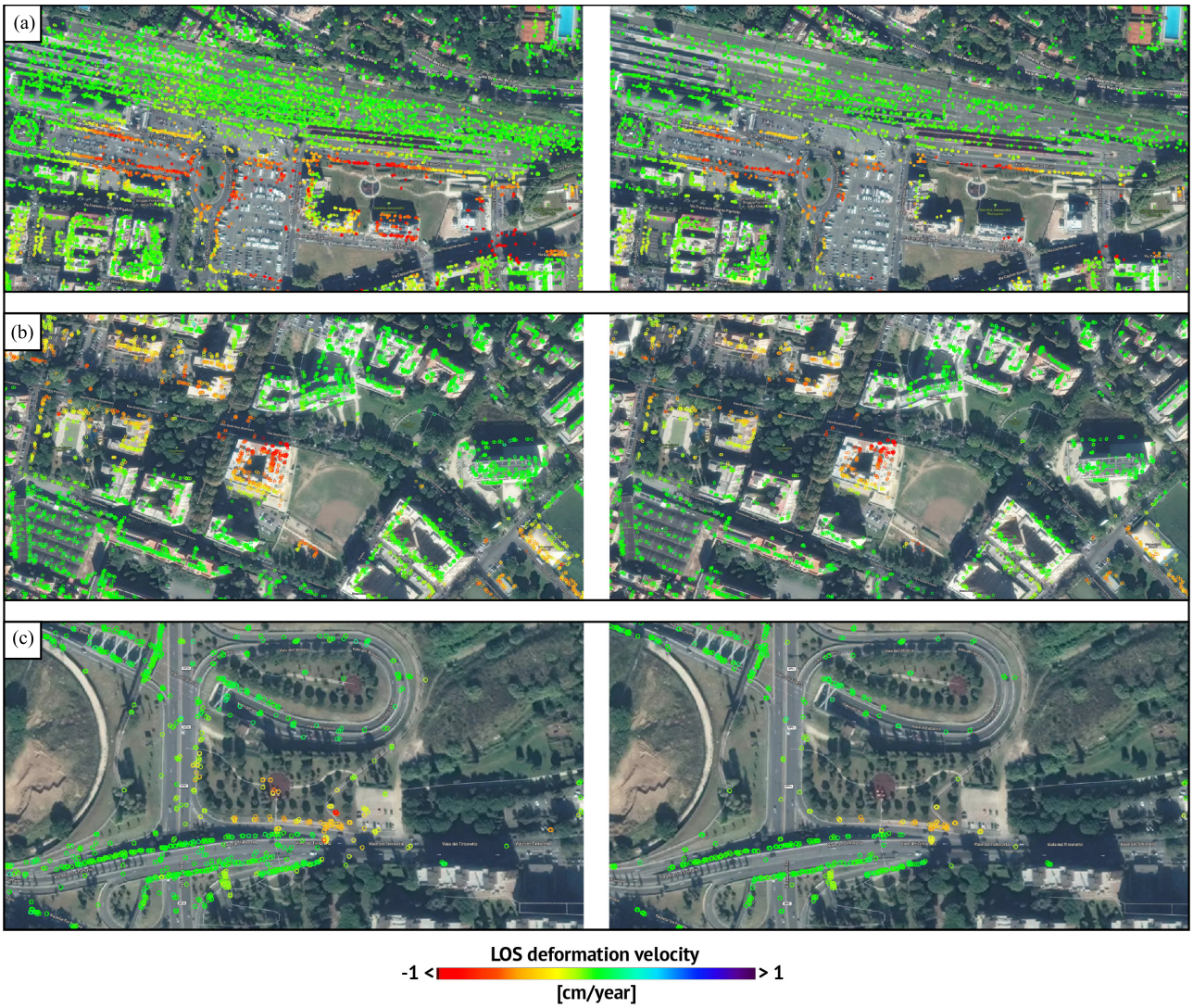

Fig. 17. Zoomed-in view of the subsiding areas referred to as (a)–(c) in Fig. 16; the LOS mean deformation velocity maps retrieved with (Left) CS-based and (Right) conventional local-scale SBAS analyses are shown.

clearly visible in the conventional analysis. This is particularly evident in the square in front of the Ostiense station and the structures around there [see Fig. 17(a)], in some buildings of Fig. 17(b), and in the park of Fig. 17(c), where a subsidence phenomenon is underway. In this latter case, the CS-enhanced approach detects several coherent points in correspondence with the center of the park, where the conventional analysis does not provide any coherent points and significantly increases the number of points along the borders of the area interested by the subsidence phenomenon.

As further analysis, we concentrate on the archeological sites located in Palatino Hill and its surroundings (see Fig. 18). In this area, we can measure some very localized deformation phenomena affecting entire structures or single portions, not visible in the results achieved with the conventional FR SBAS approach, already pointed out in previous investigations carried out in other works [44], [61], [62]. In particular, we detect displacements signals in correspondence of the Arch of Titus (P1 in Fig. 18), Temple of Venus and Roma (P2 in Fig. 18), the outer border of Roman Forum (P3 in Fig. 18), and Domus Aurea (P4 in Fig. 18). For each of these sites, a deformation time series is shown in Fig. 18.

As a final analysis, we assess the capability of the CS-based local-scale SBAS approach in retrieving nonlinear deformation signals. To this aim, we focus our analysis on some metallic structures particularly sensitive to temperature variations. In particular, we investigate the southern zone of the city where a metallic gasometer and several other metallic structures are located [see Fig. 19(a) and (c)]. On these structures, we carry out two different processing by using in both cases the CS-enhanced local-scale SBAS chain. In the first experiment, we modify the linear model by introducing in (25), as done for the azimuthal position of the scatterers in [37], an additional phase term dependent on the temperature difference between master and slave acquisitions [63], [64]. The thermal dilation component is estimated together with the other linear terms and subtracted before processing the nonlinear component. The result of such analysis is shown

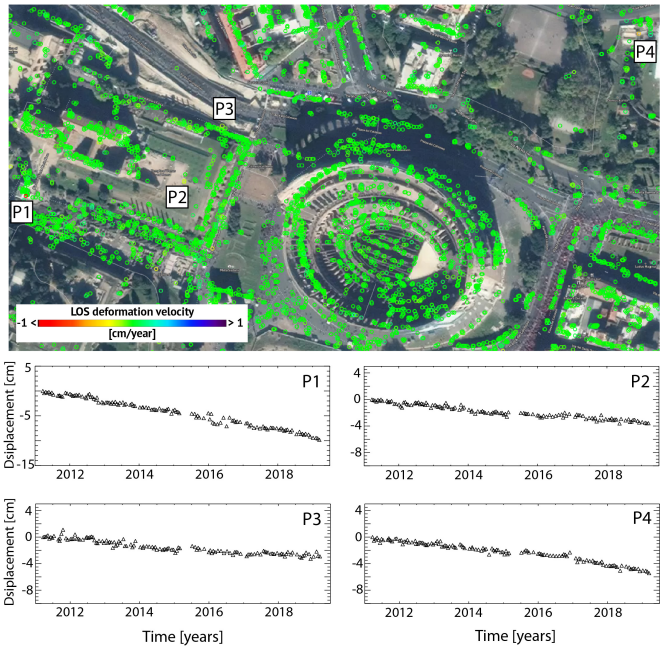

Fig. 18. (Top) LOS mean deformation velocity map, geocoded on an optical image, of the archeological sites and surrounding area around Palatino Hill. Pixels P1, P2, P3, and P4 correspond to Arch of Titus, Temple of Venus and Roma, the outer border of Roman Forum, and Domus Aurea, respectively. (Bottom) Deformation time series of the selected four pixels.

in Fig. 19(b). We detect several structures having a temporal behavior correlated with the temperature variations and characterized by thermal dilation coefficients ranging in the interval ± 1 mm/°C [see Fig. 19(b)], which corresponds to a peak–peak displacement of ± 7 rad for an X-Band SAR system and a temperature variation of about 35 °C. In the second experiment, we do not estimate the thermal dilation component together with the linear model and leave such a phase term to be estimated as nonlinear signal term; it is, therefore, retrieved as a generic nonlinear phase term by applying the CS-based algorithm presented in Section IV without benefitting from any *a priori* information (recorded temperatures). In another way, we intend to perform an experiment with real data similar to the sinusoidal curve simulated in Section V-A (fifth row in Figs. 7 and 8). The results of the two analyses are finally compared to assess their agreement and the limits of the proposed CS algorithm.

Fig. 20(a) shows the thermal dilation coefficients estimated through (left) the linear model and (right) the CS algorithm, whereas, in Fig. 20(b), the deformation time series related to some relevant points belonging to the gasometer and the closer metallic structures are shown. It is worth noting that the achieved deformation time series takes into account only for the thermal dilation and nonlinear components; the other terms coming from the regional- and local-scale analyses (e.g., atmospheric phase screen and mean deformation velocity) have not been added since they do not change between the two experiments.

By visual inspection of Fig. 20(a), it is evident that the number of coherent points achieved in the second experiment is significantly smaller because the points characterized by large thermal dilation coefficients have not been correctly unwrapped. In particular, in the second experiment, the largest values of the estimated thermal dilation coefficients are about ± 0.45 mm/°C, corresponding to a peak–peak displacement of about 6.5 rad (1.6 cm). This result is fully in agreement with the simulated data analysis carried out in a noise-free scenario (see Fig. 8), where the considered sinusoidal behavior had a peak–peak value of 8 rad. In Fig. 20(b), the retrieved deformation time series of 3 pixels with a thermal coefficient around 4 mm/°C is shown. The first column is relevant to the results of the first experiment (enhanced linear model), whereas the CS-based experiment results are reported in the second column and their difference in the third one. The almost perfect agreement between the results of the two experiments is evident, and even more relevant, the points with large PhU errors have been properly discarded. This latter result is really appreciable when applying L_1-norm minimization methods because these approaches rarely guarantee the unicity and the convergence of the solution; accordingly, the development of proper quality assessment functions plays a key role in the use of L_1-norm minimization methods in real application domains.

D. Computing Time Analysis

As a final analysis, we deal with the assessment of the computational efficiency of the proposed approach. It is worth noting that, as the proposed method represents an additional processing step to be included within the conventional multi-temporal DInSAR approaches, its computing time has to be added to the overall conventional chain processing time.

The proposed method includes several operations, but it is worth remarking that from the computational point of view the heaviest one is the L_1-norm estimation. Indeed, as said in Section II, no analytical expression to solve L_1-norm optimization problems exists; however, these can be effectively tackled by utilizing solvers based on linear programming or iterative methods. In particular, in this work, we benefit from the IRLS method that is based on an L_2-norm solution iterated with a weight function. Accordingly, the following computational time analysis deals with the performance of the IRLS method that we implemented by using MATLAB version R2020a, which is widely used throughout the scientific community.

The core operations performed within the IRLS algorithm consist of two matrix inversions and four matrix multiplications, along with two vector operations (element-by-element multiplication) for each iteration. The algorithm performs a number of iterations until either convergence is achieved or the maximum number of iterations is exceeded; therefore, its computing time changes point-by-point depending on the amount of PhU errors of the input unwrapped interferometric dataset. Finally, as the size of the matrices involved in the L_1-norm estimation depends on the number of triangles and interferograms of the Delaunay network, the problem complexity grows with the number of acquisitions of the dataset.

To assess the IRLS computing time, we use the Sentinel-1 dataset already presented in this section, composed of 171 acquisitions paired in 478 interferograms;

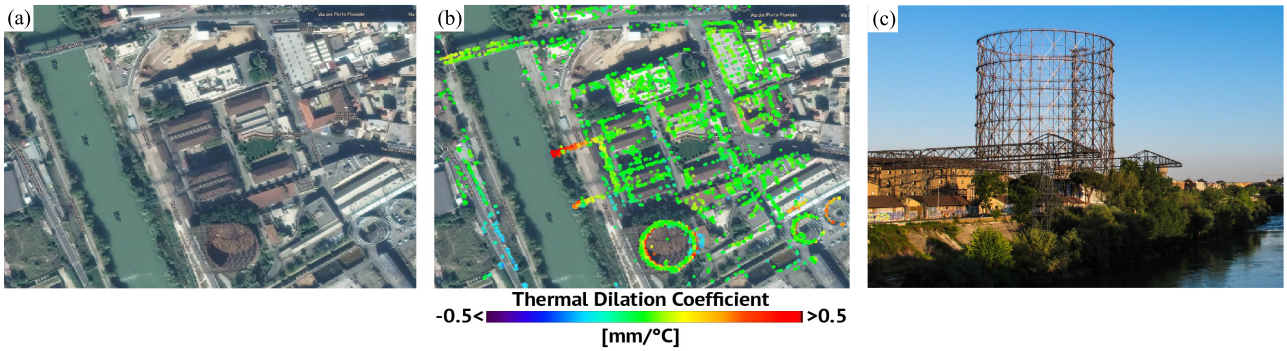

Fig. 19. Zoomed-in view of area located in the southern part of the city of Rome where several metallic structures are placed. (a) Optical image related to the analyzed area. (b) Thermal dilation coefficient map estimated the enhanced formulation of the linear model. (c) Photography relevant to the metallic gasometer located in the area.

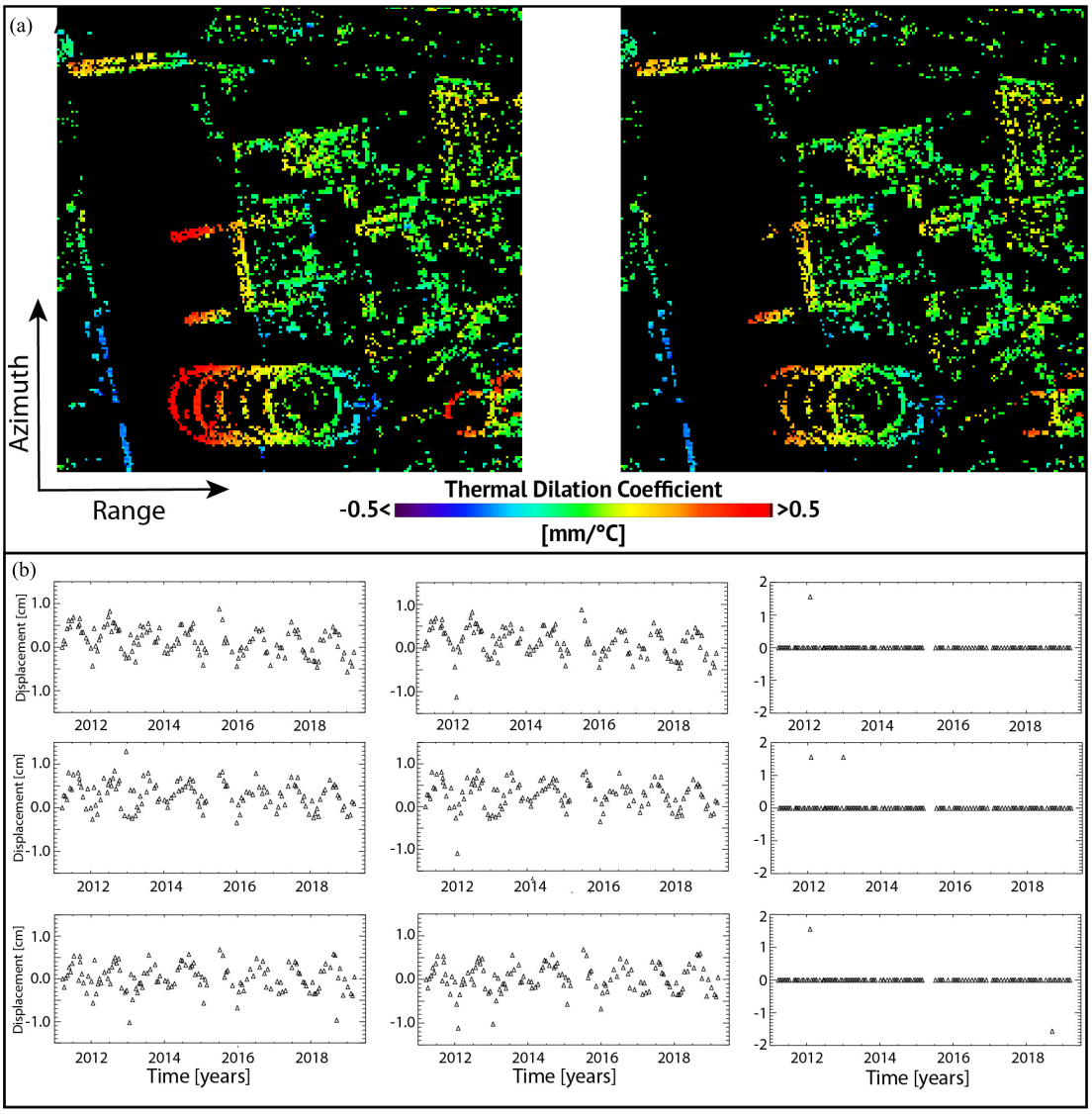

Fig. 20. Experimental results of the thermal dilation coefficient estimation. (a) Comparison between the thermal dilation coefficient maps estimated with (Left) enhanced linear model and (Right) CS-based PhU errors' retrieval algorithm. (b) Deformation time series of some pixels relevant to the metallic gasometer and other metallic structures. The three columns represent (Left to Right) results with the enhanced linear model, the CS-based algorithm, and their difference.

the corresponding Delaunay network includes 308 triangles. We estimate that, on average, ten iterations were needed in the S-1 experimental analysis presented in Section V-B to converge toward the solution. Assuming these numbers as a use case, we estimate that our MATLAB implementation of the IRLS method takes approximately 25 s to analyze

TABLE I
COMPUTATIONAL TIME ANALYSIS

Method	Average computational time for 1000 pixels [sec]
Lauknes	~14
Khwaja	~1540
Our method	~25

1000 points (roughly corresponding to 7 h for an area of 1000 × 1000 pixels). In Table I, the computing time of the proposed method is compared with those achieved for the Lauknes' and Khwaja's approaches presented in [18] and [20], respectively. For the implementation of the *Huber*-norm optimization operation applied in Khwaja's method, we used the CVX package [65], [66], whereas Lauknes' approach was implemented with the IRLS routine. The three tests have been carried out on an Apple MacBook Pro 13" equipped with a quad-core Intel i7 CPU (2.3 GHz) and 32 GB of RAM.

VI. CONCLUSION

In this article, we presented a solution based on CS theory to mitigate the PhU errors in the multitemporal sequence of differential interferograms exploited by the advanced DInSAR methods. In particular, the developed CS-based algorithm receives as input the unwrapped interferometric stack and estimates the PhU errors by retrieving, for each pixel, the sparse vector that solves the triangulated network built in the temporal/spatial baseline plane. We tailored our approach to the SBAS processing chain to estimate and correct the PhU errors that may affect FR SBAS results. In particular, we enhanced both the regional- and local-scale SBAS processing chains with a new module that retrieves the PhU errors of the sequence of exploited differential interferograms by searching for a minimum L_1-norm solution. We demonstrated that CS can be effectively used to retrieve PhU errors although a unique sparse minimum L_1-norm solution cannot be always retrieved. To improve the robustness of the proposed approach, we modified the L_1 estimator, based on the IRLS method, by changing the weight function that now takes into account the temporal interferometric baselines. This enhancement significantly improves the performance in retrieving the PhU errors that can be originated by significant nonlinear deformation signals. Finally, to limit false alarm issues and discard unreasonable solutions, we developed a quality assessment function based on the phase residuals of the interferometric pairs. The developed method was successfully assessed both on simulated and real data. In particular, two SAR datasets, acquired over Central Italy in the last ten years by Sentinel-1 and CSK constellations, were used to validate the proposed CS-based algorithm with the regional- and local-scale SBAS results. The achieved experimental results clearly confirm the capability of the enhanced CS-based SBAS processing chain to effectively reconstruct nonlinear deformation time series; this relevant achievement is clearly shown by better recovering, with respect to the conventional SBAS chain, the deformation signals relevant to the three main shocks of the 2016 Italian seismic sequence, and the FR thermal dilation displacements relevant to several metallic structures located within the city of Rome.

The main drawback of the proposed approach concerns the computational load and the processing time. Converse to L_2 methods, there is no analytical expression for L_1-norm minimization algorithms, and the CS reconstruction approaches are mainly based on linear programming strategies and iterative methods, whose complexity and computational load are significantly larger than L_2 analytical methods. To overcome this drawback, advanced parallel computing techniques could be used. For example, as the algorithm is applied on a pixel-by-pixel basis, an effective way to easily speed up the procedure is to compute different groups of pixels with different cores/CPUs. Likewise, the exploitation of graphic processing units (GPUs) is an effective way to significantly reduce computing time.

Considering the huge flow of SAR data coming from the existing (e.g., Sentinel-1, COSMO-SkyMed, and TerraSAR-X) and incoming systems (NISAR), it will be highly beneficial to investigate the computational optimization of the developed CS-based PhU errors' retrieval algorithm, by also taking advantage of high-performance computing (HPC) and cloud computing environments.

ACKNOWLEDGMENT

The authors would like to thank European Commission, Copernicus Programme, and ESA for the systematic six-day Sentinel-1 data acquisition and their open data policy. COSMO-SkyMed (CSK) SAR data were acquired through the Italian Space Agency and the Italian Civil Protection Department Agreement; the digital elevation models of the analyzed areas were acquired through the NASA SRTM archive. This article contains modified Copernicus Sentinel data 2021. The authors would also like to thank the editors and the anonymous reviewers for their valuable suggestions that have helped to improve the quality of this article.

REFERENCES

[1] A. K. Gabriel, R. M. Goldstein, and H. A. Zebker, "Mapping small elevation changes over large areas: Differential radar interferometry," *J. Geophys. Res.*, vol. 94, no. B7, pp. 9183–9191, Jul. 1989.

[2] P. A. Rosen *et al.*, "Synthetic aperture radar interferometry," *Proc. IEEE*, vol. 88, no. 3, pp. 333–382, Mar. 2000.

[3] R. Bamler and P. Hartl, "Synthetic aperture radar interferometry synthetic aperture radar interferometry," *Inverse Problems*, vol. 14, no. 4, p. 55, 1998.

[4] P. Berardino, G. Fornaro, R. Lanari, and E. Sansosti, "A new algorithm for surface deformation monitoring based on small baseline differential SAR interferograms," *IEEE Trans. Geosci. Remote Sens.*, vol. 40, no. 11, pp. 2375–2383, Nov. 2002.

[5] R. Lanari, O. Mora, M. Manunta, J. J. Mallorqui, P. Berardino, and E. Sansosti, "A small-baseline approach for investigating deformations on full-resolution differential SAR interferograms," *IEEE Trans. Geosci. Remote Sens.*, vol. 42, no. 7, pp. 1377–1386, Jul. 2004.

[6] A. Ferretti, C. Prati, and F. Rocca, "Nonlinear subsidence rate estimation using permanent scatterers in differential SAR interferometry," *IEEE Trans. Geosci. Remote Sens.*, vol. 38, no. 5, pp. 2202–2212, Sep. 2000.

[7] A. Ferretti, C. Prati, and F. Rocca, "Permanent scatterers in SAR interferometry," *IEEE Trans. Geosci. Remote Sens.*, vol. 39, no. 1, pp. 8–20, Jan. 2001.

[8] C. Werner, U. Wegmüller, T. Strozzi, and A. Wiesmann, "Interferometric point target analysis for deformation mapping," in *Proc. IEEE Int. Geosci. Remote Sens. Symp. (IGARSS)*, Jul. 2003, pp. 4362–4364.

[9] O. Mora, J. J. Mallorquí, and A. Broquetas, "Linear and nonlinear terrain deformation maps from a reduced set of interferometric SAR images," *IEEE Trans. Geosci. Remote Sens.*, vol. 41, no. 10, pp. 2243–2253, Oct. 2003.

[10] A. Hooper, H. Zebker, P. Segall, and B. Kampes, "A new method for measuring deformation on volcanoes and other natural terrains using InSAR persistent scatterers," *Geophys. Res. Lett.*, vol. 31, no. 23, Dec. 2004, Art. no. L23611.

[11] A. Ferretti, A. Fumagalli, F. Novali, C. Prati, F. Rocca, and A. Rucci, "A new algorithm for processing interferometric data-stacks: SqueeSAR," *IEEE Trans. Geosci. Remote Sens.*, vol. 49, no. 9, pp. 3460–3470, Sep. 2011.

[12] M. Crosetto, B. Crippa, and E. Biescas, "Early detection and in-depth analysis of deformation phenomena by radar interferometry," *Eng. Geol.*, vol. 79, nos. 1–2, pp. 81–91, Jun. 2005.

[13] A. Pepe, L. D. Euillades, M. Manunta, and R. Lanari, "New advances of the extended minimum cost flow phase unwrapping algorithm for SBAS-DInSAR analysis at full spatial resolution," *IEEE Trans. Geosci. Remote Sens.*, vol. 49, no. 10, pp. 4062–4079, Oct. 2011.

[14] H. Yu, Y. Lan, Z. Yuan, J. Xu, and H. Lee, "Phase unwrapping in InSAR," *IEEE Geosci. Remote Sens. Mag.*, vol. 7, no. 1, pp. 40–58, Mar. 2019.

[15] Y. Yang, A. Pepe, M. Manzo, F. Casu, and R. Lanari, "A region-growing technique to improve multi-temporal DInSAR interferogram phase unwrapping performance," *Remote Sens. Lett.*, vol. 4, no. 10, pp. 988–997, Oct. 2013.

[16] C. Ojha, M. Manunta, A. Pepe, L. Paglia, and R. Lanari, "An innovative region growing algorithm based on minimum cost flow approach for phase unwrapping of full-resolution differential interferograms," in *Proc. IEEE Int. Geosci. Remote Sens. Symp.*, Jul. 2012, pp. 5582–5585.

[17] Z. Yunjun, H. Fattahi, and F. Amelung, "Small baseline InSAR time series analysis: Unwrapping error correction and noise reduction," *Comput. Geosci.*, vol. 133, pp. 1–19, Dec. 2019.

[18] T. R. Lauknes and H. A. Zebker, "InSAR deformation time series using an L_1 norm small-baseline approach," *IEEE Trans. Geosci. Remote Sens.*, vol. 49, no. 1, pp. 536–546, Jan. 2011.

[19] X. Xu and D. T. Sandwell, "Toward absolute phase change recovery with InSAR: Correcting for Earth tides and phase unwrapping ambiguities," *IEEE Trans. Geosci. Remote Sens.*, vol. 58, no. 1, pp. 726–733, Jan. 2020.

[20] A. S. Khwaja and M. Cetin, "Improved DInSAR time-series reconstruction in the presence of phase unwrapping errors using Huber-norm," *IET Radar, Sonar Navigat.*, vol. 13, no. 7, pp. 1063–1073, Jul. 2019.

[21] H. A. Zebker and J. Villasenor, "Decorrelation in interferometric radar echoes," *IEEE Trans. Geosci. Remote Sens.*, vol. 30, no. 5, pp. 950–959, Sep. 1992.

[22] M. Rani, S. B. Dhok, and R. B. Deshmukh, "A systematic review of compressive sensing: Concepts, implementations and applications," *IEEE Access*, vol. 6, pp. 4875–4894, 2018.

[23] D. L. Donoho, "Compressed sensing," *IEEE Trans. Inf. Theory*, vol. 52, no. 4, pp. 1289–1306, Apr. 2006.

[24] B. K. Natarajan, "Sparse approximate solutions to linear systems," *SIAM J. Comput.*, vol. 24, no. 2, pp. 227–234, Apr. 1995.

[25] M. R. Garey and D. S. Johnson, *Computers and Intractability: A Guide to the Theory of NP-Completeness* (A Series of Books in the Mathematical Sciences). San Francisco, CA, USA: Freeman, 1979, p. 338.

[26] V. M. Patel, G. R. Easley, D. M. Healy, and R. Chellappa, "Compressed synthetic aperture radar," *IEEE J. Sel. Topics Signal Process.*, vol. 4, no. 2, pp. 244–254, Apr. 2010.

[27] M. T. Alonso, P. López-Dekker, and J. J. Mallorqui, "A novel strategy for radar imaging based on compressive sensing," *IEEE Trans. Geosci. Remote Sens.*, vol. 48, no. 12, pp. 4285–4295, Dec. 2010.

[28] X. X. Zhu and R. Bamler, "Super-resolution power and robustness of compressive sensing for spectral estimation with application to space-borne tomographic SAR," *IEEE Trans. Geosci. Remote Sens.*, vol. 50, no. 1, pp. 247–258, Jan. 2012.

[29] X. X. Zhu and R. Bamler, "Tomographic SAR inversion by L_1-norm regularization—The compressive sensing approach," *IEEE Trans. Geosci. Remote Sens.*, vol. 48, no. 10, pp. 3839–3846, Oct. 2010.

[30] W. Pu, Y. Huang, J. Wu, H. Yang, and J. Yang, "Fast compressive sensing-based SAR imaging integrated with motion compensation," *IEEE Access*, vol. 7, pp. 53284–53295, 2019.

[31] J. Fang, Z. Xu, B. Zhang, W. Hong, and Y. Wu, "Fast compressed sensing SAR imaging based on approximated observation," *IEEE J. Sel. Topics Appl. Earth Observ. Remote Sens.*, vol. 7, no. 1, pp. 352–363, Jan. 2014.

[32] F. Casu, M. Manzo, and R. Lanari, "A quantitative assessment of the SBAS algorithm performance for surface deformation retrieval from DInSAR data," *Remote Sens. Environ.*, vol. 102, nos. 3–4, pp. 195–210, Jun. 2006.

[33] M. Bonano, M. Manunta, A. Pepe, L. Paglia, and R. Lanari, "From previous C-band to new X-band SAR systems: Assessment of the DInSAR mapping improvement for deformation time-series retrieval in urban areas," *IEEE Trans. Geosci. Remote Sens.*, vol. 51, no. 4, pp. 1973–1984, Apr. 2013.

[34] Y. Morishita, M. Lazecky, T. Wright, J. R. Weiss, J. R. Elliott, and A. Hooper, "LiCSBAS: An open-source InSAR time series analysis package integrated with the LiCSAR automated Sentinel-1 InSAR processor," *Remote Sens.*, vol. 12, p. 424, Jan. 2020.

[35] F. Casu, M. Manzo, A. Pepe, and R. Lanari, "SBAS-DInSAR analysis of very extended areas: First results on a 60 000-km^2 test site," *IEEE Geosci. Remote Sens. Lett.*, vol. 5, no. 3, pp. 438–442, Jul. 2008.

[36] C. De Luca, I. Zinno, M. Manunta, R. Lanari, and F. Casu, "Large areas surface deformation analysis through a cloud computing P-SBAS approach for massive processing of DInSAR time series," *Remote Sens. Environ.*, vol. 202, pp. 3–17, Dec. 2017.

[37] M. Bonano, M. Manunta, M. Marsella, and R. Lanari, "Long-term ERS/ENVISAT deformation time-series generation at full spatial resolution via the extended SBAS technique," *Int. J. Remote Sens.*, vol. 33, no. 15, pp. 4756–4783, Aug. 2012.

[38] M. Corsetti, F. Fossati, M. Manunta, and M. Marsella, "Advanced SBAS-DInSAR technique for controlling large civil infrastructures: An application to the Genzano di Lucania dam," *Sensors*, vol. 18, no. 7, p. 2371, Jul. 2018.

[39] L. Solari *et al.*, "Combined use of C- and X-band SAR data for subsidence monitoring in an urban area," *Geosciences*, vol. 7, no. 2, p. 21, Apr. 2017.

[40] S. Scifoni *et al.*, "On the joint exploitation of long-term DInSAR time series and geological information for the investigation of ground settlements in the town of Roma (Italy)," *Remote Sens. Environ.*, vol. 182, pp. 113–127, Sep. 2016.

[41] D. Notti *et al.*, "A user-oriented methodology for DInSAR time series analysis and interpretation: Landslides and subsidence case studies," *Pure Appl. Geophys.*, vol. 172, no. 11, pp. 3081–3105, Mar. 2015.

[42] R. Castaldo *et al.*, "Landslide kinematical analysis through inverse numerical modelling and differential SAR interferometry," *Pure Appl. Geophys.*, vol. 172, no. 11, pp. 3067–3080, Nov. 2015.

[43] S. Arangio, F. Calò, M. Di Mauro, M. Bonano, M. Marsella, and M. Manunta, "An application of the SBAS-DInSAR technique for the assessment of structural damage in the city of Rome," *Struct. Infrastruct. Eng. Maintenance, Manage. Life-Cycle Des. Perform.*, vol. 10, pp. 1–15, Oct. 2013.

[44] G. Zeni *et al.*, "Long-term deformation analysis of historical buildings through the advanced SBAS-DInSAR technique: The case study of the city of Rome, Italy," *J. Geophys. Eng.*, vol. 8, no. 3, pp. S1–S12, Sep. 2011.

[45] C. De Luca *et al.*, "An on-demand Web tool for the unsupervised retrieval of Earth's surface deformation from SAR data: The P-SBAS service within the ESA G-POD environment," *Remote Sens.*, vol. 7, no. 11, pp. 15630–15650, Nov. 2015.

[46] T. R. Lauknes, A. P. Shanker, J. F. Dehls, H. A. Zebker, I. H. C. Henderson, and Y. Larsen, "Detailed rockslide mapping in northern Norway with small baseline and persistent scatterer interferometric SAR time series methods," *Remote Sens. Environ.*, vol. 114, no. 9, pp. 2097–2109, Sep. 2010.

[47] F. Casu *et al.*, "SBAS-DInSAR parallel processing for deformation time-series computation," *IEEE J. Sel. Topics Appl. Earth Observ. Remote Sens.*, vol. 7, no. 8, pp. 3285–3296, Aug. 2014.

[48] M. Manunta *et al.*, "The parallel SBAS approach for Sentinel-1 interferometric wide swath deformation time-series generation: Algorithm description and products quality assessment," *IEEE Trans. Geosci. Remote Sens.*, vol. 57, no. 9, pp. 6259–6281, Sep. 2019.

[49] I. Zinno *et al.*, "National scale surface deformation time series generation through advanced DInSAR processing of Sentinel-1 data within a cloud computing environment," *IEEE Trans. Big Data*, vol. 6, no. 3, pp. 558–571, Sep. 2020.

[50] E. J. Candes, J. Romberg, and T. Tao, "Robust uncertainty principles: Exact signal reconstruction from highly incomplete frequency information," *IEEE Trans. Inf. Theory*, vol. 52, no. 2, pp. 489–509, Feb. 2006.

[51] A. Pepe and R. Lanari, "On the extension of the minimum cost flow algorithm for phase unwrapping of multitemporal differential SAR interferograms," *IEEE Trans. Geosci. Remote Sens.*, vol. 44, no. 9, pp. 2374–2383, Sep. 2006.

[52] A. S. Bandeira, E. Dobriban, D. G. Mixon, and W. F. Sawin, "Certifying the restricted isometry property is hard," *IEEE Trans. Inf. Theory*, vol. 59, no. 6, pp. 3448–3450, Jun. 2013.

[53] A. Bastounis and A. C. Hansen, "On the absence of uniform recovery in many real-world applications of compressed sensing and the restricted isometry property and nullspace property in levels," *SIAM J. Imag. Sci.*, vol. 10, no. 1, pp. 335–371, Jan. 2017.

[54] C. S. Burnus, "Iterative reweighted least squares, version 12," OpenStax CNX, Houston, TX, USA, Tech. Rep., Nov./Dec. 2012.

[55] M. Costantini and P. A. Rosen, "Generalized phase unwrapping approach for sparse data," in *Proc. Int. Geosci. Remote Sens. Symp. (IGARSS)*, 1999, pp. 267–269.

[56] G. Lavecchia *et al.*, "Ground deformation and source geometry of the 24 August 2016 Amatrice earthquake (Central Italy) investigated through analytical and numerical modeling of DInSAR measurements and structural-geological data," *Geophys. Res. Lett.*, vol. 43, no. 24, pp. 389–398, Dec. 2016.

[57] D. Cheloni *et al.*, "Geodetic model of the 2016 Central Italy earthquake sequence inferred from InSAR and GPS data," *Geophys. Res. Lett.*, vol. 44, pp. 6678–6787, Jul. 2017.

[58] M. Manunta, M. Marsella, G. Zeni, M. Sciotti, S. Atzori, and R. Lanari, "Two-scale surface deformation analysis using the SBAS-DInSAR technique: A case study of the city of Rome, Italy," *Int. J. Remote Sens.*, vol. 29, no. 6, pp. 1665–1684, Mar. 2008.

[59] S. Stramondo *et al.*, "Subsidence induced by urbanisation in the city of Rome detected by advanced InSAR technique and geotechnical investigations," *Remote Sens. Environ.*, vol. 112, no. 6, pp. 3160–3172, Jun. 2008.

[60] M. Delgado, M. Foumelis, C. Stewart, and A. Hooper, "Measuring urban subsidence in the Rome metropolitan area (Italy) with Sentinel-1 SNAP-StaMPS persistent scatterer interferometry," *Remote Sens.*, vol. 11, pp. 129, Jan. 2019.

[61] F. Cigna, R. Lasaponara, N. Masini, P. Milillo, and D. Tapete, "Persistent scatterer interferometry processing of COSMO-SkyMed StripMap HIMAGE time series to depict deformation of the historic centre of Rome, Italy," *Remote Sens.*, vol. 6, no. 12, pp. 12593–12618, Dec. 2014.

[62] D. Tapete, R. Fanti, R. Cecchi, P. Petrangeli, and N. Casagli, "Satellite radar interferometry for monitoring and early-stage warning of structural instability in archaeological sites," *J. Geophys. Eng.*, vol. 9, no. 4, pp. S10–S25, Aug. 2012.

[63] O. Monserrat, M. Crosetto, M. Cuevas, and B. Crippa, "The thermal expansion component of persistent scatterer interferometry observations," *IEEE Geosci. Remote Sens. Lett.*, vol. 8, no. 5, pp. 864–868, Sep. 2011.

[64] D. Reale, G. Fornaro, and A. Pauciullo, "Extension of 4-D SAR imaging to the monitoring of thermally dilating scatterers," *IEEE Trans. Geosci. Remote Sens.*, vol. 51, no. 12, pp. 5296–5306, Dec. 2013.

[65] M. Grant and S. Boyd. *CVX: MATLAB Software for Disciplined Convex Programming, Version 2.0 Beta*. Accessed: Feb. 10, 2021. [Online]. Available: http://cvxr.com/cvx

[66] M. Grant and S. Boyd, "Graph implementations for nonsmooth convex programs," in *Recent Advances in Learning and Control* (Lecture Notes in Control and Information Sciences), V. Blondel, S. Boyd, and H. Kimura, Eds. London, U.K.: Springer, 2008, pp. 95–110.

Michele Manunta was born in Cagliari, Italy, in 1975. He received the Laurea degree in electronic engineering and the Ph.D. degree in informatics and electronic engineering from the University of Cagliari, Cagliari, in 2001 and 2009, respectively.

Since 2002, he has been with the Istituto per il Rilevamento Elettromagnetico dell'Ambiente (IREA)-Italian National Research Council (CNR), Naples, Italy, where he is a Researcher. He was a Visiting Scientific with the Institut Cartogràfic i Geològic de Catalunya, Catalonia, Spain, in 2004, and the Rosenstiel School of Marine and Atmospheric Science, University of Miami, Coral Gables, FL, USA, in 2006. He has been contributing to various national and international initiatives for the exploitation of satellite technologies and, in particular, synthetic aperture radar (SAR) techniques. He has been coordinating the satellite component of the EPOS research infrastructure, where he holds the role of TCS Satellite Data Director. His research interests are in the field of high-resolution SAR and differential interferometric SAR (DInSAR) data processing and application. He particularly works on developing SAR/DInSAR algorithms and techniques for studying deformation affecting terrain surface and man-made structures. More recently, his research interests concern cloud and GRID computing exploitation for SAR interferometry applications.

Muhammad Yasir was born in Wah Cantt., Pak-istan, in 1988. He received the bachelor's degree in electronics and the master's degree in computer vision and machine learning from Quaid-i-Azam University, Islamabad, Pakistan, in 2011 and 2015, respectively. He is pursuing the Ph.D. degree with the University of Naples "Parthenope," Naples, Italy.

He joined Istituto per il Rilevamento Elettromagnetico dell'Ambiente (IREA)-Italian National Research Council (CNR), Naples, in 2019. His research interests are in the field of high-resolution synthetic aperture radar (SAR) and differential interferometric SAR (DInSAR) data processing and applications. He particularly works on developing SAR/DInSAR algorithms and techniques for studying deformation affecting terrain surface and man-made structures.